Monitoring based intelligent perception and prediction of vortex-induced vibration of long-span bridges: methodology and application

Danhui Dan[a,b], Xuewen Yu[a,*], Houjin Li[a], Gang Zeng[a], Chenqi Wang[a] and Hua Guan[c]

[a]*College of Civil Engineering, Tongji University, Shanghai, 200092, China*

[b]*Key Laboratory of Performance Evolution and Control for Engineering Structures of Ministry of Education, Tongji University, Shanghai, 200092, , China*

[c]*Zhengjiang Zhoushan Sea Crossing Bridge Co., Ltd., Zhoushan, 316031, Zhejiang, China*

ARTICLE INFO

ABSTRACT

With the continuous breakthrough in span and the application of lightweight and high-strength materials, bridge structures have become increasingly flexible, highlighting the issue of wind-induced vibrations. Among them, vortex-induced vibration (VIV) occurs under frequent wind conditions and is difficult to avoid entirely. This article first briefly reviews the research on bridge VIV from three perspectives: mechanism and modeling, monitoring and perception, and control and utilization. Subsequently, the focus is concentrated on the intelligent perception and prediction of bridge VIV, presenting an integral methodology system including (a) Real-time identification of VIV based on the features of structural responses; (b) Online tracking of structural state parameters when VIV occurs; (c) Assessment of driving comfort and safety during VIV based on vibration level and field of view; (d) Prediction of VIV driven by data rules and dynamical model. This technical framework covers the whole chain consisting of VIV prediction, identification, tracking, and evaluation, which can provide timely data support for bridge management and maintenance. The article utilized the VIV events of two long-span suspension bridges to demonstrate the effectiveness of the proposed methods. And some of these methods have been applied to construct a VIV monitoring system for one of the bridges and have achieved sound effects. This paper offers a relatively comprehensive technical framework and practical experience for VIV perception and prediction of long-span bridges and other engineering structures or components prone to VIV, such as cables, high-rise buildings, and offshore wind turbines.

1. Introduction

Vortex-induced vibration (VIV) is a common phenomenon observed in engineering practices, particularly in slender and flexible structures or components, such as the main girder [1, 2, 3, 4, 5, 6, 7, 8, 9] and cables [10, 11] of long-span bridges, chimneys [12], towers [13], wind turbines [14, 15, 16], marine risers [17, 18], floating tunnels [19]. From the mechanical perspective, VIV can be regarded as a supercritical Hopf bifurcation [20, 21], characterized by stable limit cycles. In other words, this type of vibration exhibits self-limiting behavior and will not directly cause structural collapse. Nevertheless, frequent and sustained large-scale vibrations pose a risk of exacerbating structural fatigue damage and affecting the usage performance and even functionality of structures. For instance, as for bridges, significant VIV not only impacts the driver's experience [22, 23] but also has the potential to necessitate traffic restrictions on the bridge deck [4, 3, 2], thereby impeding the normal operation of economic and social activities.

The studies on bridge VIV broadly encompass the following aspects: (1) elucidating the underlying mechanism of VIV and establishing models of the force caused by vortex excitation; (2) monitoring VIV occurrences and gaining insights into the structural condition; and (3) implementing strategies for mitigating large-amplitude VIV response and harnessing the energy it generates.

---

*Corresponding author

✉ dandanhui@tongji.edu.cn (D. Dan);
xuewen_yu@tongji.edu.cn (X. Yu); 1932246@tongji.edu.cn (H. Li);
gangzengtj@gmail.com (G. Zeng); wangchenqi@tongji.edu.cn (C. Wang); gh_1983@hotmail.com (H. Guan)
    ORCID(s): 0000-0003-4774-7139 (X. Yu)

1.1. Mechanism and modeling of VIV

The general principle of VIV is well-known and can be described as follows: Under certain flow conditions, flow separation leads to the formation of alternating vortex shedding (known as the Von Kármán vortex street) and the generation of corresponding vortex-induced forces (VIFs) acting on the structure. Simultaneously, due to the fluid-structure interaction (FSI), resonance occurs when the shedding frequency of vortices approaches a certain order of structural frequency (lock-in), triggering significant self-excited vibrations. However, to reveal the VIV mechanism of a bridge with the specific structural type and cross-sectional shape, thorough investigations of conditions leading to vortex shedding, vortex occurrence locations, and vortex evolutionary process are necessary, which are crucial for providing theoretical guidance on suppressing VIV.

During structural design, it is usually to enhance the aerodynamic performance of the structure through optimizations of section configuration and implementations of constructional measures, aiming at inhibiting or disrupting the formation and development of vortices. And as a result, the probability of VIV occurrence can be reduced, and the peak amplitude of VIV response can be mitigated [24]. The design is a trial-and-error process that requires (numerical) wind tunnel tests for verification. Computational fluid dynamics (CFD) provides an economical and convenient means for precise and rapid VIV simulation and for design verification. Frandsen [25] used the finite element method (FEM) and discrete vortex method (DVM) to numerically simulate the VIV of the Great Belt East suspension bridge in Denmark. The results showed that flow separation occurred at the leading edge, converting downstream along the surface of the main beam and alternately shedding in the wake. Lima et al. [26] investigated the effects of attachments (handrails, crash barriers, wind barriers, and maintenance railings) on the aerodynamic characteristics and VIV responses of a twin-box girder through experimental models. The results demonstrated that attachments would cause large leading flow separation. Wu et al. [27] measured the wind pressure, structural response, and wake during VIV through wind tunnel tests, and compared the sectional wind pressure distribution and the frequency characteristic of vortex shedding under different combinations of auxiliary components.

Establishing accurate mathematical models for VIF is the prerequisite for reliable prediction of VIV response. In the 1980s and 1990s, Scanlan et al. proposed the linear empirical model [28] and the nonlinear empirical model [29]. The latter can simulate the characteristics of self-excitation and self-limiting of VIV by introducing a nonlinear aerodynamic damping force (expressed as the product of displacement squared and velocity). On this basis, Larsen introduced a shape parameter to adjust the order of nonlinear aerodynamic damping force (expressed as the product of displacement to any power and velocity), proposing a generalized nonlinear empirical model. These empirical models are formally equivalent to the Van der Pol-type oscillator [30]. Zhu et al. revealed the limitations of Scanlan and Larsen's models in certain bridge sections, such as closed box deck and centrally slotted box deck. They proposed that the nonlinear aerodynamic damping force term should primarily depend on velocity rather than displacement and introduced a cubic velocity term [31, 32, 33]. Building upon this insight, they developed a more general VIF model represented as a complete higher-order bivariate (velocity, displacement) polynomial. In practice, a simplified model is derived by ignoring non-dominant force terms [34, 35], which shares a similar form with the Duffing oscillator. The parameters in the above models are generally determined through wind tunnel tests. In addition, Wu and Kareem employed the truncated Volterra series [36] to simulate the VIF, which also captures the typical characteristics of VIV [37, 38]. Xu et al. [39] utilized the Volterra theory-based reduced-order modeling technique to simulate the fluid-structure coupling of the bridge deck under VIV. The kernel of the Volterra series was identified from the input-output pairs of CFD calculations using the least squares method (LSM) and considering the kernel's sparsity.

In recent years, there has been considerable research interest in the direct discovery of physical laws or governing equations from data [40, 41, 42, 43, 44]. These approaches belong to a kind of regression model for data fitting. Li et al. [45] applied the sparse identification of nonlinear dynamics (Sindy) algorithm to discover the time-varying dynamical equation from measured wind speed and acceleration data. Moreover, Ma et al. [46] employed the Sindy algorithm to identify the nonlinear aerodynamic force of the quasi-flat plate, incorporating group sparsity regularization to account for the fact that control equations in similar cases share

the same form. They showed that regularization enhances the accuracy and reliability of the identification results.

The realistic mechanism of VIV will be complicated due to the individual cross-sectional form exhibited by the bridge and the changing flow field. Thus, a generic expression of the VIF model may contain multiple force terms spanning a wide range of orders and characterized by sparse coefficients, where the distribution and values of these coefficients are contingent upon the specific circumstances. In light of this, the data-driven method is equivalent to the parameter identification of time-varying systems and is highly adaptable. Such an approach is beneficial to revealing underlying laws from the detailed depiction of historical data. But it is hard to make long-term predictions for the current dynamic system. Conversely, empirical models offer a more generalized perspective and can give rough estimates of the system evolution, which is very important in some scenarios.

1.2. Monitoring and perception

At the design stage, although a series of measures were taken to suppress the VIV response and ensure compliance with the standards, long-span bridges still experience VIV with excessive amplitude in reality. The reasons behind this may be: Firstly, due to the complexity and variability of the VIV occurrence mechanism, the passive structural measures adopted in the design phase cannot cope with all possible triggering factors of VIV. Secondly, the cross-sectional configuration of the structure may undergo unexpected changes during operation, leading to unfavorable aerodynamic profiles. These changes may result from modifications to the attachments of the bridge, the influence of moving vehicles/convoys on the bridge deck, and the uncertainty of the cross-sectional attitude. For example, in May 2020, the Humen Bridge in China experienced VIVs due to the disruption of the streamlined aerodynamic shape of the main girder caused by the temporary placement of water horses on the bridge deck, resulting in a maximum amplitude of approximately 0.3 m [3, 2]. Similarly, in October 2014, the Yi Sun-sin Bridge in South Korea encountered VIVs due to the reduction of the aerodynamic performance caused by the temporary covering of the guardrail with a curtain used for maintaining and curing the epoxy-coated road surface that just replaced, leading to a maximum amplitude of 0.52 m [6]. Additionally, because the standard concentrates on transient behavior, much large amplitude (but still lower than the threshold) VIVs are allowed. However,

once the VIV develops and reaches a stable stage, such significant vibrations will persist for quite a long time, ranging from tens of minutes to hours, and therefore deserve sufficient attention. Table 1 lists some notable VIV events of long-span bridges worldwide.

For bridges in operation, structural health monitoring (SHM) technology [51, 52, 53] provides a means to identify VIV and track the structural status in real-time, thereby enabling bridge managers to respond to VIV events promptly and scientifically. At present, many long-span bridges have been equipped with SHM system [54, 55, 56, 57], which generally includes the measurement of acceleration, wind speed, and other contents, sufficient to meet the requirements of monitoring VIV. On this basis, many scholars have studied VIV utilizing field and full-scale measurements.

Li et al. [58] proposed a fast clustering algorithm to identify VIV events from long-term monitoring datasets, where acceleration amplitude and frequency ratio were selected as features for clustering. Huang et al. [59] introduced an automatic method for identifying VIV responses based on the random decrement technique (RDT). The authors found that the RDT-processed acceleration data exhibited different characteristics between VIV and regular random vibrations and defined a peak coefficient of variation as the threshold to distinguish these two responses. Xu et al. [60] performed a detailed analysis of wind field and vibration acceleration data measured from a suspension bridge from 2014 to 2016. They finally selected four parameters, namely average wind speed, wind direction, the root of mean squares (RMS) of acceleration, and frequency ratio, to construct the criterion for determining VIV occurrence. The identification rate was 89% on the test of monitoring data in 2017. Zhao et al. [7] proposed a rapid warning method for bridge VIV driven by multi-source monitoring data. Dan and Li [50] utilized the uni-modal characteristics of VIV response and proposed an index using recursive Hilbert transform, which can indicate the development status of VIV in real-time and calculate key parameters such as instantaneous frequency, phase, and amplitude during VIV. Lim et al. [61] trained a deep neural network (DNN) using labeled datasets to classify vibration responses and detect the occurrence of VIV. Zhang et al. [62] observed the VIV of a long-span suspension bridge using non-contact sensing measurements such as microwave radar, optical camera, and video equipment. They determined the features between the bridge dynamical characteristics and VIV responses,

Table 1
Summary of some VIV events of long-span bridges (a certain VIV event for each bridge).

Bridge	Type	MS (m)	Time	D (h)	A (m)	F (Hz)	WS (m/s)
Trans-Tokyo Bay Crossing Bridge, Japan	I	2×240	Jul, 1995 [5]	≈1	0.54	0.340	13~18
Second Severn Crossing Bridge, UK	II	456	Dec, 1996 [47]	≈2	0.22	0.326	15~20
Great Belt Bridge, Denmark	III	1624	Apr, 1998 [48]	≈1	0.25	0.130	4~12
The Second Jindo Bridge, South Korea	II	344	Apr, 2011 [49]	≈2	0.19	0.438	9.8~11.5
Volgograd Bridge, Russia	I	7×155	May, 2010 [4]	≈4	0.36	—	11.6~15.6
Xihoumen Bridge, China	III	1650	2011~2014 [9]	≈3	0.17	0.327	10.2~12
Yi Sun-Shin Bridge, South Korea	III	1545	Oct, 2014 [6]	≈2	0.52	0.318	5.3~7.0
Yingwuzhou Bridge, China	III	2×850	Apr, 2020 [7]	≈1	—	0.244	5~10
Humen Bridge, China	III	888	May, 2020 [50]	≈2	0.12	0.227	2.5~7.5

[a] Type: I for continuous bridge, II for cable-stayed bridge; III for suspension bridge.

[b] MS, D, A, F and WS mean Main Span, Duration, Amplitude, Frequency and Wind Speed, respectively.

[c] — means not clear.

i.e., single-mode vibration and dominant mode switching. Thus, they proposed a VIV warning scheme based on vibration frequency and similarity between bridge configuration and modal shapes. Li et al. [63] presented a recurrent neural network (RNN)-based deep learning framework to identify the relationship between VIV amplitude and wind speed from on-site monitoring data. They incorporated residual connections in the network to simulate the ordinary differential equation (ODE) [64, 65], which gave a kind of dynamics interpretation to the network structure.

In addition, due to the issues such as size effects, accurately simulating the realistic flow field is challenging, so wind tunnel tests and numerical simulations cannot reflect the VIV in full fidelity. The field measurements of the full-scale bridge are effective supplements to investigating the mechanisms of VIV and validating the accuracy of empirical VIF models. Li et al. [9] studied 37 VIV events observed in a twin-box girder suspension bridge and discovered that apart from wind direction and incoming turbulence, the inhomogeneity of the wind field along the span direction of the bridge is also a key factor affecting the VIV of the full-size bridge. For the same bridge, Zhu et al. [66] compared the VIV responses of the prototype bridge calculated by their proposed empirical VIF model with that measured in the field, and the study indicated that turbulence could efficiently suppress VIV responses in low-frequency mode, and the nonuniform distribution of the mean wind speed can also help reduce VIV

responses. However, the impact of the nonuniform distribution of turbulence is negligible. Liu et al. [67] introduced a Bayesian inference method to identify the VIF parameters from the field measurements, which obtained more accurate estimates than wind tunnel tests.

SHM system also provides a way to handle VIV and evaluate the corresponding effects. Ge et al. [2] and Zhao et al. [3] utilized monitoring data to conclude that the primary cause of sustained VIV in Humen Bridge was the reduction of mechanical damping, and thus decided to install a tuned mass damper (TMD) to improve the structural damping performance. And subsequently, a significant decrease in VIV amplitude was observed. Kim et al. [68] conducted a comparative analysis of VIV responses and damping ratios before and after the installation of a multiple TMD (MTMD) for a cable-stayed bridge affected by VIVs, to assess the suppressive effect of MTMD.

1.3. Control and utilization

Once VIV occurs (at this point, all measures taken in the design stage failed), the amplitude gradually grows until it stabilizes. Unless marked changes appear in the flow field, it is difficult for the vibration to naturally subsides. In order to ensure structural safety and maintain smooth traffic flow, active or passive control of the VIV is necessary. For the VIV control of existing bridges, there are two main ideas. One is to modify the local flow field around the bridge to prevent

energy input, such as by increasing or retrofitting the auxiliary facilities [69, 70] and employing suction/jet devices [71, 72, 73]. The second is to help the structure dissipate energy, such as installing TMD [74, 75, 76].

Xin et al. [69] proposed an inclined railing with improved pillars inspired by passive vortex generators (PVG). The flow vortices developed downstream of the PVG pillar can trigger the three-dimensional instability of the wake, preventing the shear layer from getting involved in a mature vortex street. Based on the same principle, Zhan et al. [70] proposed a new passive control device called wave railing to mitigate the VIV response of a single-box girder. Xue et al. [71] proposed an active flow control method, the external suction and blow method, which is achieved by cyclically arranging suction and blowing devices on the lower surface of the bridge. Zheng et al. (2021) developed an adaptive flow control scheme that utilizes a pair of jets placed at the poles of a cylinder as actuators, combined with active learning and reinforcement learning for real-time feedback control. Implicit physics suggests that jets contain suction during the vortex generation stage and injection during the vortex shedding stage. Chen et al. [73] conducted an experimental study to examine the control effectiveness and potential mechanisms of the leading-edge suction and trailing-edge jet (LSTJ) of a box beam with a Reynolds number of 2.08×10^4, confirming the control effectiveness of LSTJ under various wind attack angles.

Dai et al. [74] investigated the optimal design of a Maxwell tuned-mass-damper-inerter (MTMDI) for mitigating the VIV of bridges. Yu et al. [75] considered four VIF models and systematically analyzed the influence of different VIF models on the design of TMDs for controlling VIV. Dai et al. [77] proposed a technique for controlling bridge VIV using an active TMD (ATMD), where the control algorithm is independent of bridge parameters and allows real-time adjustment of bridge motion with minimal measurements. Patil et al. [76] employed multi-objective optimization to find the Pareto-optimal solution for suppressing VIV using multiple manners simultaneously, effectively addressing the conflict objectives between performance and cost in a highly nonlinear design space. However, when controlling VIV, careful attention should be paid to whether the measures taken would make the structure inclined to exhibit other wind-induced vibrations, especially for divergent ones such as flutter [78, 2].

Over recent years, research on energy harvesting from flow-induced vibrations has gradually progressed and matured. Researchers have developed various types of energy harvesters to collect environmental wind energy, water energy, structure mechanical energy [79, 80, 81, 82, 83, 84], and so on. These energy harvesters hold promising applications in bridge structures prone to VIVs. According to the energy conversion mechanisms, energy harvesters are classified into electromagnetic, piezoelectric, electrostatic, dielectric, triboelectric, and hybrid types. They can not only absorb VIV energy to reduce vibration but also provide clean power to the micro-electro-mechanical system (MEMS) and wireless sensor system of the SHM system. This is a further development of purely energy-consuming VIV control. Farhangdoust et al. [85] proposed an efficient linear and nonlinear energy harvesting system for wireless monitoring of a long-span cable-supported bridge. And the simulation results demonstrated that the captured energy is sufficient to power the sensors of the bridge monitoring systems.

1.4. Our work

The reviewed research contents in Sections 1.1~1.3 are interconnected and are summarized in Figure 1 as follows: Firstly, the study of VIV mechanisms and VIF models serves as a guide for designing VIV control and energy harvesting devices (Figure 1(a) → 1(c)). Secondly, the monitoring and perception of VIV can trigger and instruct the controller to act, and the control effect is evaluated and fed back through the recognition results of the monitoring system. Additionally, the captured vibration energy is used to power the monitoring system (Figure 1(b) ↔ 1(c)). Thirdly, the monitoring and perception of VIV are employed to verify the reasonability of structural design and the applicability of the empirical VIF model. The on-site measurements can be directly utilized to study the specific causes of VIV and construct the mathematical model of VIF (Figure 1(b) → 1(a)). It is evident that the study of VIV monitoring and perception plays a top-down role in this

$$1(a) \longleftarrow 1(b) \longleftrightarrow 1(c)$$
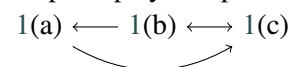
research closure: .

This paper focuses on the monitoring and perception of bridge VIV. Building partly upon the authors' previous work [50], we propose a full-process, multifaceted methodological framework for VIV perception and prediction. The framework consists of two main aspects: (1) Real-time identification, tracking, and evaluation of VIV (perception) based on the measured acceleration signals. Specifically, we construct an index for distinguishing VIV events based on the uni-modal characteristic of VIV responses. We present methods
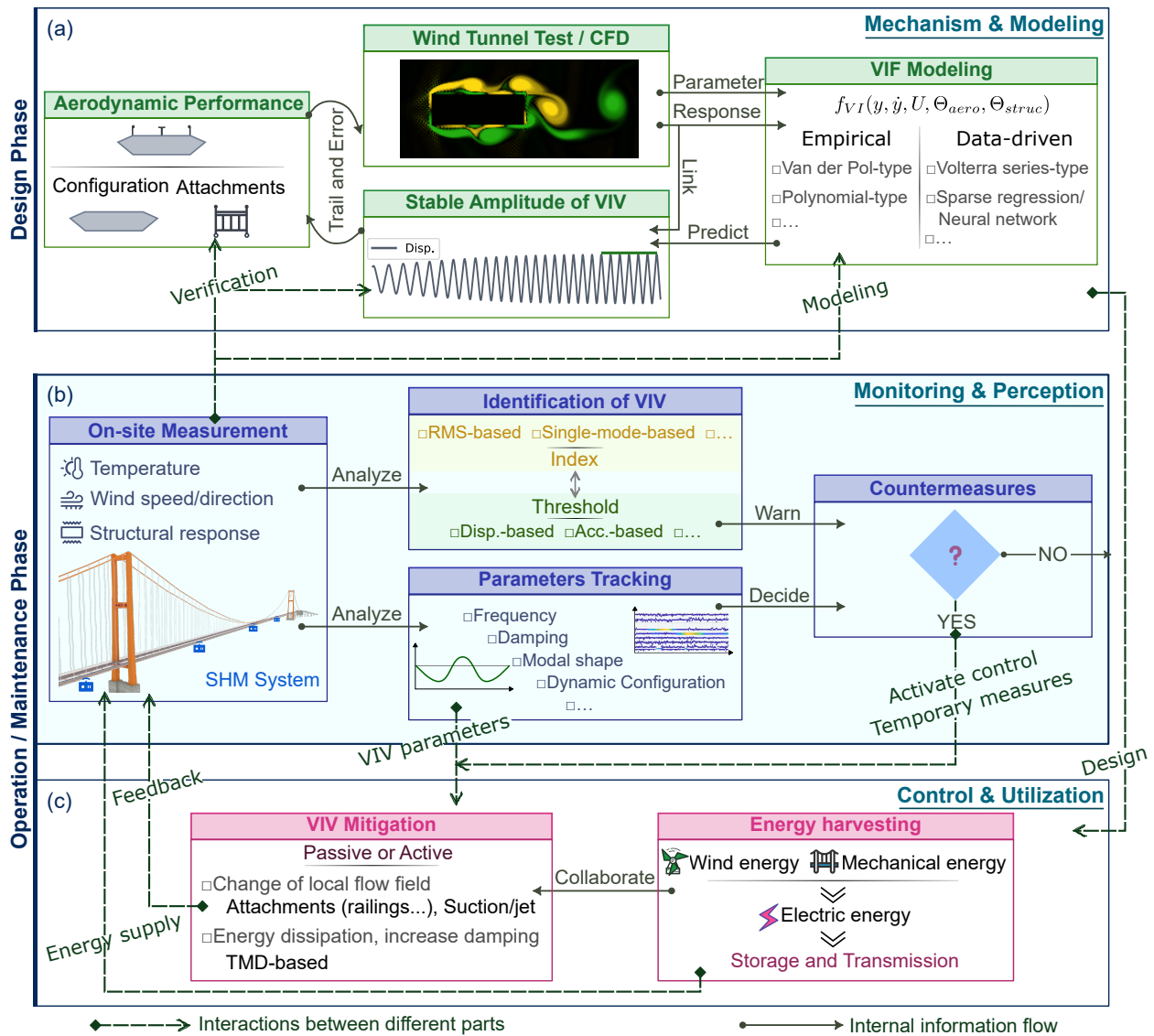
Figure 1: Research loop of bridge VIV. (a) Mechanism and modeling. (b) Monitoring and perception. (c) Control and utilization.

for calculating structural state parameters and assessing ride comfort and safety during VIV. (2) Probability prediction of VIV triggered by measured wind speeds. It includes the VIV occurrence prediction driven by statistical rules and a neural network and VIV stable amplitude estimation driven by a dynamical model. The proposed methods are applied to analyze the monitoring data of two long-span suspension bridges, confirming their feasibility and effectiveness. In particular, the VIV identification and tracking techniques have been utilized to construct a VIV monitoring system for one of the bridges. The system has been operating for nearly two years and successfully identified and tracked multiple VIV events, providing timely data support for bridge management and maintenance.

The article is organized as follows: Section 2 provides a detailed introduction to the methodological system for monitoring-based VIV perception and prediction. Section 3 examines the effectiveness of the proposed methods in the context of two actual suspension bridges and presents the application of the VIV monitoring system construction for one of the bridges. Section 4 discusses some relevant issues. Finally, Section 5 concludes the whole paper and explores future research directions.

The main contributions of this paper are:

⌐ proposes a comprehensive technical framework for intelligent perception and prediction of bridge VIV;

Table 2
Definitions and characteristics of different periods and moments of VIV division.

Period	Moment	Definition	Main characteristic
A←--B		Pre-VIV	Vehicle-induced vibration dominated
	B	Wind field-locked	
BC		Embryonic period	Vortex-shedding, fluid-structure interaction
	C	Occurrence of VIV in response	
CD		Development period	Frequency-locked, negative-damping
	D	Reach a stable state	
DE		Stable period	Input/output balance, zero-damping
	E	Start to decay	
EF		Decaying period	Energy dissipation, positive-damping
	F	End of VIV	
F--→G		Post-VIV	Vehicle-induced vibration dominated

⌋ offers specific method implementations for each functional aspect of the framework, covering VIV identification, tracking, assessment, and prediction;

⌋ verifies the effectiveness of the proposed methods using measured data from two long-span suspension bridges;

⌋ builds and deploys a VIV monitoring system based on the proposed methods on top of the existing SHM system for one of the bridges.

2. The methodology system of VIV perception and prediction

2.1. General framework

As shown in Figure 2(a), we divide the time history of structural response (typically acceleration) into six different periods according to its features. These periods are named pre-VIV (A←--B), embryonic period (BC), development period (CD), stable period (DE), decaying period (EF), and post-VIV (F--→G). The pre-/post-VIV periods correspond to the non-VIV periods dominated by vehicle-induced vibrations. The embryonic period signifies the formation of specific wind field conditions, with the onset of vortex shedding and gradual strengthening of FSI. The development period means that the vortex frequency has locked in, and the characteristic of VIV can be detected in the response signal. The stable period implies zero total damping, with energy input and output reaching dynamic equilibrium, forming a limit cycle with a stable amplitude. The decaying period indicates the disruption of the equilibrium state, gradual dissipation of accumulated

energy, and restoration of normal vibration levels. Definitions and main characteristics of the above periods and moments are presented in Table 2.

VIV is an abnormal vibration pattern that can be observed deterministically from the structural response. We can judge the occurrence of VIV by utilizing the distinct characteristics exhibited in the structural response under VIV and non-VIV. On the other hand, structural VIV does not occur instantaneously. It happens under specific wind conditions (e.g., appropriate wind speed, attack angle, etc.), where the environmental wind continuously inputs energy into the structure due to the periodic vortex shedding and the fluid-structure coupling effect. This energy input needs to last for a while to excite the VIV of the whole bridge. Thus the characteristics of wind will manifest before that of structural response when VIV is going to happen, which implies the possibility of predicting VIV occurrence (result) in advance by monitoring the wind field features (cause). Therefore, as shown in Figure 2(b), in the framework of VIV perception and prediction, we propose a structural response-based VIV identification-tracking-evaluation route and a wind field-based VIV prediction route. Among them, the main parts include:

1. **VIV identification**: During the full-time period (AG), extract a VIV index from the response signal in real-time and compare it with the threshold to determine whether VIV occurs. The purpose is to detect VIV at its early stage when the structural vibration level is still relatively small (moment C).

2. **VIV tracking**: Once VIV is detected, identification of modal parameters (e.g., frequency,
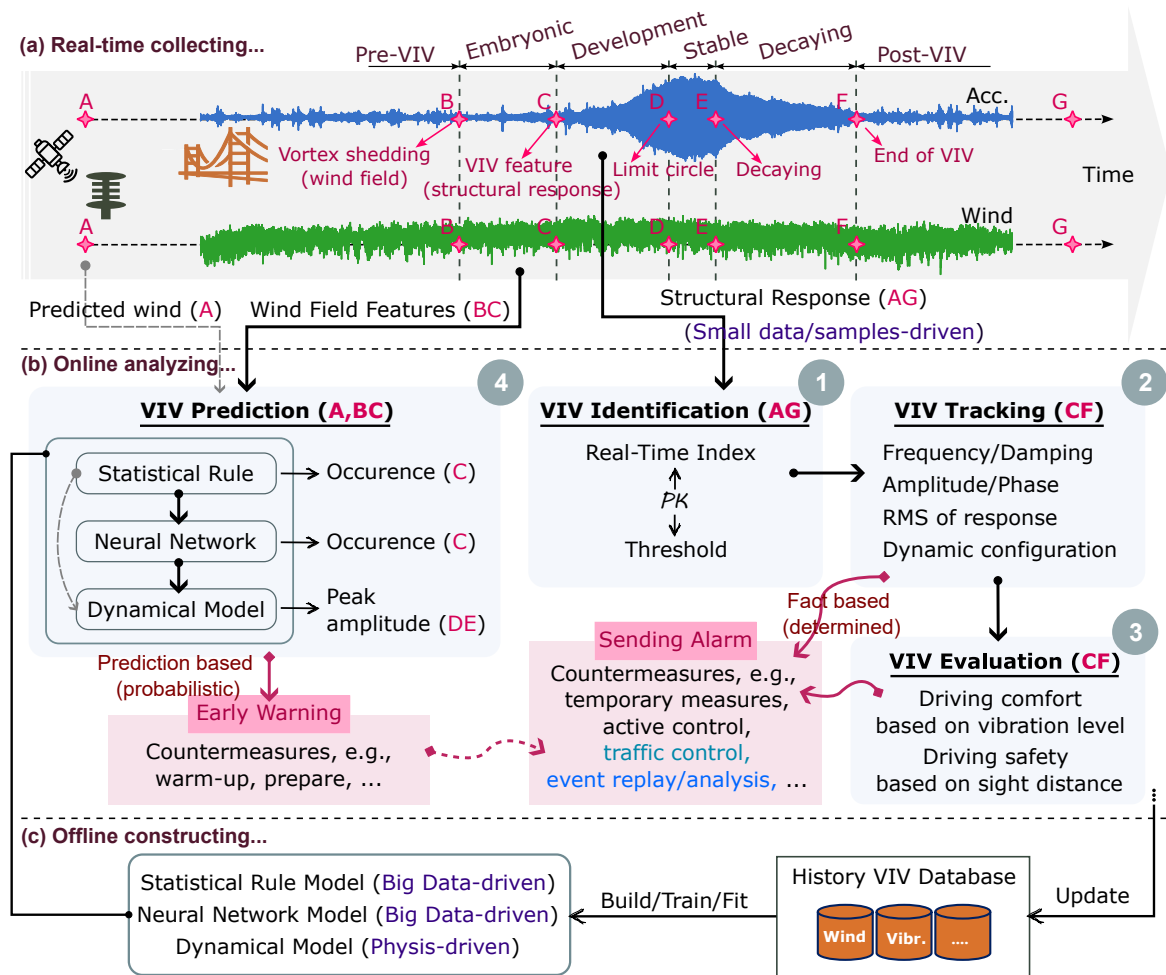
Figure 2: General framework of intelligent perception and prediction of bridge VIV.

damping, modal shape) and status parameters (e.g., RMS of response, amplitude/phase, dynamic configuration) of the structure is carried out during VIV (CF). These parameters can be used to guide the control of VIV. For example, the frequency and modal order can help determine the parameter settings for active and passive control, and the RMS value and amplitude information can provide insights into the structural motion state.

3. **VIV evaluation**: Meanwhile, the assessment of driving on the bridge deck during VIV (CF) is performed from two aspects: estimate the driving comfort based on the vibration level of the structure; evaluate the driving safety in terms of the driver's field of view. These rely on the calculation of the vibration shape of the full bridge during VIV.

4. **VIV prediction**: There are two ways to realize this purpose: The first one, termed long-term prediction, is to predict the wind speed and direction at the bridge site in the next few hours (moment A) using meteorological station observation data such as high-resolution satellite cloud images. Then compare the predicted wind with the statistical rule of wind characteristics at the time of VIV to determine whether VIV is likely to occur. The second one, termed short-term prediction, is to employ a neural network model to predict the trend of the VIV index at the embryonic period (BC) and then judge whether VIV will occur. In both ways, the stable amplitude can be calculated by a structural dynamic model. Currently, long-term prediction faces many challenges due to the difficulties in obtaining corresponding meteorological data, the inadequate spatial resolution of wind observation stations, low accuracy in long-range prediction of random
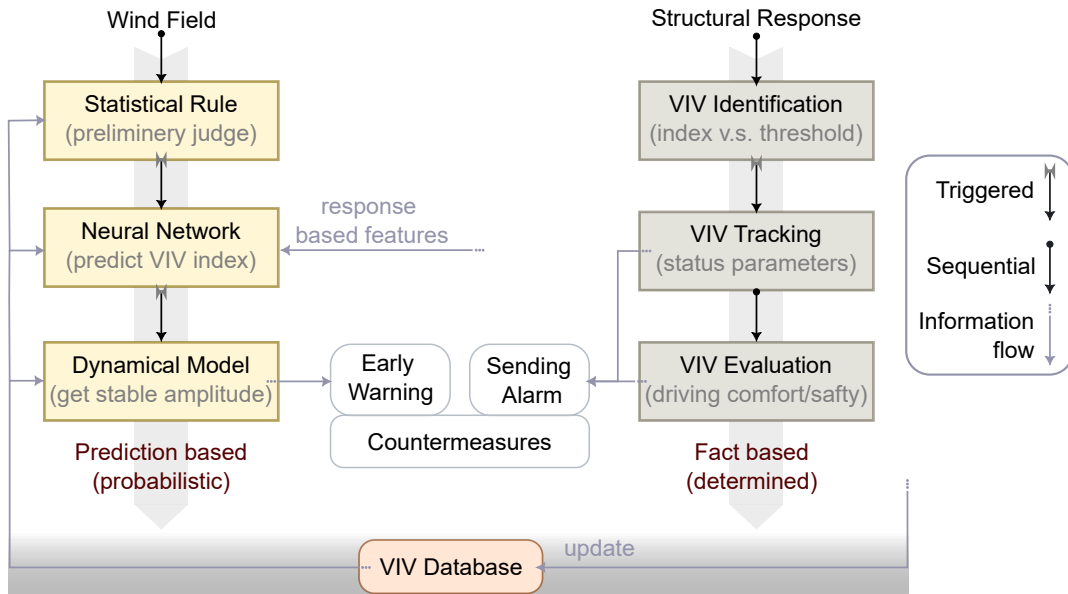
Figure 3: Execution logic of the proposed framework.

wind fields, and unclear guidance for practical bridge maintenance. Therefore, this paper only presents this conceptual route without more specific discussion.

The logical associations of different parts in the framework are as follows (Figure 3): In the offline phase, VIV events are automatically extracted from the raw monitoring data using the proposed VIV identification method to build the VIV database (Figure 2(c)). Then utilizing the database to derive the statistical rules of wind field characteristics corresponding to VIVs, train the neural network model to predict the trend of VIV indicator, and fit the parameters in the dynamical model. In the online phase, on the one hand (left side of Figure 3), calculating real-time wind field characteristics and using the statistical rule to determine if the wind locked to the range of VIV. If so, start the neural network to predict the tendency of the VIV index. Once the predicted index exceeds the threshold, it is determined that a VIV will occur. At the same time, applying the dynamical model to estimate the stable amplitude will be reached and issuing an early warning. According to the prediction results, take corresponding countermeasures such as emergency preparedness. On the other hand (right side of Figure 3), calculate the VIV index in real-time from the measured accelerations. Once the index exceeds the set threshold, an occurrence of VIV is confirmed. Start tracking the key structural state/modal parameters and evaluating the driving comfort and safety of the

bridge. Then, send an alarm carried with the tracked and evaluated information to comprehensively taking the final measures. When each VIV event ends, the VIV database is supposed to be updated to keep it improved and up-to-date. In this logical framework, continuous calculations are required for wind field characteristics and the VIV index, while the rest of the calculation tasks are triggered based on the two, which can significantly reduce the demand for computing resources. The methods involved in this technical framework are described individually in the following sections.

2.2. VIV real-time identification

The core of identifying VIV events from structural response signals is to construct an index that can accurately distinguish the cases of VIV and non-VIV. Represent the response $y(t)$ at a certain measurement point on the structure as the sum of K harmonic components and assume that the frequency remains constant within a short time window:

$$y(t) = \sum_{k=1}^{K} A_k(t) \cos\left(\omega_k t + \phi_k\right) + \epsilon(t), \quad (1)$$

where, $A_k(t)$ represents the instantaneous amplitude; ω_k stands for the vibration frequency; ϕ_k denotes the initial phase; and $\epsilon(t)$ corresponds to the noise. When VIV occurs, the vibration energy primarily concentrates on a specific vibration mode due to lock-in, resulting in a uni-modal response, i.e., $\bar{A}_{k_{VIV}} \gg \bar{A}_{k_{oths}}$. Here, $k_{VIV} \in \{1, 2, \cdots, K\}$ is the index of dominant VIV mode, whereas $k_{oths} \in \{1, 2, \cdots, K\} \setminus k_{VIV}$ is the

index of the other mode, and $\bar{A}_k$ denotes the average amplitude over a certain period. Conversely, under regular environmental excitation (non-VIV period), the energy distribution of the structural responses spans multiple modes and is time-varying. Consequently, the overall structural response manifests as a multi-modal random vibration.

We have constructed a discriminant index based on the uni-modal characteristics of VIV response, referred to as the R index [50]. Compared with vibration energy-based indicators such as RMS of response and other indicators based on uni-modal characteristics, the R index has the following advantages: simplicity in calculations, strong universality, independence from the modal order, structural form, and measurement point location, and can identify both large-scale and small-scale VIV. The calculation process is as follows: (1) obtain the real-time displacement by integrating the acceleration twice; (2) perform the Hilbert transform (HT) of the displacement to obtain the analytic signal; (3) calculate the VIV index using the instantaneous amplitude of the analytic signal. To make this paper self-consistent, the following briefly describes this method in our previous work [50].

2.2.1. Integration of dynamic displacement

The structural response measured by the SHM system is generally acceleration, $a(t)$. The dynamic displacement, $d(t)$, can be obtained by integrating $a(t)$ twice. Since the initial displacement and velocity are unknown at the time of integration, baseline calibration is necessary while also considering the influence of noise.

The whole integration process is expressed as:

$$\check{a}(t) = \mathrm{HPF}[\mathrm{BLC}(a(t))]; \tag{2a}$$

$$v(t) = \mathrm{HPF}\{\mathrm{BLC}[\mathrm{INT}(\check{a}(t))]\}; \tag{2b}$$

$$d(t) = \mathrm{HPF}\{\mathrm{BLC}[\mathrm{INT}(v(t))]\}. \tag{2c}$$

In the above equation, BLC represents "baseline correction", which means removing the baseline (linear tendency) from the signal; HPF represents "high-pass filtering" for eliminating the long-term drift; INT represents "integration" for the first-order integration. The signals obtained by Equations 2a, 2b and 2c are calibrated acceleration, integrated and calibrated velocity, and integrated and calibrated displacement, respectively.

BLC is implemented by fitting the linear term through LSM:

$$\mathrm{BLC}(x(t)) = x(t) - (c_0 + c_1 t), \tag{3a}$$

$$c_0, c_1 = \arg \min_{c_0, c_1} \| c_0 + c_1 t - x(t) \|_2^2, \tag{3b}$$

where, c_0 and c_1 coefficients to be fitted.

HPF is expressed as the following recursive form [86, 87]:

$$\mathrm{HPF}(x(t)) = \frac{1+q}{2} (x(t) - x(t-1)) + q\mathrm{HPF}(x(t-1)), \tag{4}$$

where parameter $0 < q < 1$ controls the high-pass bandwidth. It is recommended to take values as the method in [88] to obtain optimal frequency response characteristics.

INT can be calculated by trapezoidal integration or Fourier transform:

$$\mathrm{INT}(x(t)) = \begin{cases} \frac{\Delta t}{2}(x(t-1) + x(t)), & \text{Trapezoid method,} \\ \mathcal{F}^{-1}\left\{ \frac{1}{i\omega} \mathcal{F}\{x(t)\} \right\}, & \text{Fourier method.} \end{cases} \tag{5}$$

In the above equation, Δt is the sampling interval; $\mathcal{F}$ represents Fourier transform; $\mathcal{F}^{-1}$ represents inverse Fourier transform; ω is frequency; and $i = \sqrt{-1}$.

For more details on this dynamic displacement integration method, please refer to our previous work [88].

2.2.2. Analytic signal

After obtaining the integrated dynamic displacement, its analytic form can be calculated using the HT:

$$d_{\mathrm{analyt}}(t) = d(t) + i\mathcal{H}(d)(t) = \sum_{k=1}^{K} A_k(t) \exp(i(\omega_k t + \varphi_k)), \tag{6}$$

where $\mathcal{H}$ represents the HT, which is defined using the Cauchy principal value (p.v.) as

$$\mathcal{H}(d)(t) = \frac{1}{\pi} \mathrm{p.v.} \int_{-\infty}^{+\infty} \frac{d(\tau)}{t - \tau} d\tau. \tag{7}$$

2.2.3. VIV index

Denote the amplitude (envelope) of the analytic signal in Equation 6 as $A(t) := \left| d_{\mathrm{analyt}}(t) \right|$, then the VIV index is constructed as:

$$R_{\mathrm{VIV}} = \frac{\min(A(t))}{\max(A(t))}. \tag{8}$$

Given the uni-modal feature of the structural VIV response, the corresponding analytic displacement $d_{\text{analyt}}^{\text{VIV}}(t)$ can be further expressed as:

$$d_{\text{analyt}}^{\text{VIV}}(t) = d_{\text{analyt}}(t) \approx A_{k_{\text{VIV}}}(t) \exp\left(i\left(\omega_{k_{\text{VIV}}}t + \varphi_{k_{\text{VIV}}}\right)\right), \tag{9}$$

i.e., $A(t) = A_{k_{\text{VIV}}}(t)$. Because amplitude $A_{k_{\text{VIV}}}(t)$ varies slowly with time, $A(t)$ could be regarded as a constant within a short duration. So, R_{VIV} is close to 1. While during the non-VIV phase, $A(t)$ is the envelope of multiple harmonic components, and R_{VIV} is close to 0 in this case.

The R index has the following geometric interpretation on the complex plane that is formed by the real and imaginary parts of the analytic signal (see Equation 6): During VIV, the trajectory of the uni-modal response is almost confined to a circular path (or a thin annulus), whereas for non-VIV, the trajectory of the multi-modal response nearly fills the entire circular plane (Figure 4). The R index provides a quantitative characterization of this geometric feature.
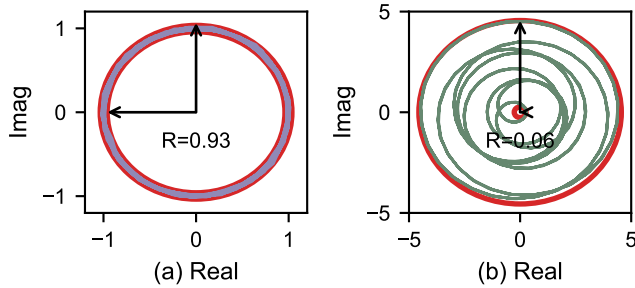
Figure 4: Illustration of VIV index: (a) Trajectory of uni-component signal simulated for VIV. (b) Trajectory of multi-components signal simulated for non-VIV.

2.3. VIV online tracking

This section aims to track the structural modal and motion parameters throughout the VIV process, once VIV occurrence is detected. Thereby grasping the vibration status of the structure in real-time and providing data support for VIV control and evaluation.

2.3.1. Amplitude, phase, frequency, and modal shape

Obviously, the vibration amplitude and phase are equal to that of analytic displacement in Equation 9:

$$A_{\text{VIV}}(t) = \left|d_{\text{analyt}}^{\text{VIV}}(t)\right|, \tag{10}$$

$$\varphi_{\text{VIV}}(t) = \angle d_{\text{analyt}}^{\text{VIV}}(t), \tag{11}$$

where $|\cdot|$ and $\angle\cdot$ return the modulus and angle of a complex number, respectively.

And the frequency is calculated as the first-order derivation of the phase:

$$\omega_{\text{VIV}}(t) = \frac{d\varphi_{\text{VIV}}(t)}{dt}. \tag{12}$$

By arranging the displacements at all sensor locations distributed along the span, we can obtain the dynamic configuration of structural vibrations. And when VIV occurs, it transfers to the corresponding modal shape:

$$\boldsymbol{\phi}_{\text{VIV}}(t) = \left[d_{\text{VIV},1}(t), \cdots, d_{\text{VIV},i}(t), \cdots, d_{\text{VIV},C}(t)\right]^{T}, \tag{13}$$

where, i is the index of sensor location; C is the number of sensors; d_{VIV} represents the VIV displacement of the ith sensor.

2.3.2. Representative damping ratio

We utilize the logarithmic decay method to compute the damping ratio during VIV (Figure 5):

$$\xi_{\text{VIV}}(t) = -\frac{1}{\omega_{\text{VIV}(t)}}\frac{d\ln A_{\text{VIV}}(t)}{dt}. \tag{14}$$

And the damping ratio at this point can be seen as a linear equivalent of the total damping of the structure, the sum of the aerodynamic damping and structural damping, and is called the representative damping ratio. As a result, the occurrence and development process of VIV can be discussed from the damping aspect.
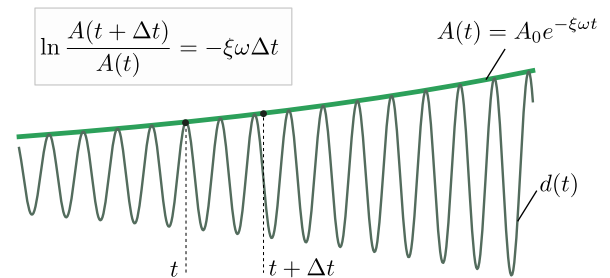
Figure 5: Logarithmic decay method for calculating representative damping ratio during VIV.

It is worth noting that Equations 10~14 are only applicable to the single-degree-of-freedom (SDOF) response during VIV. If still using them during non-VIV, it is necessary to decompose the non-VIV response into single-modal components first, which can be realized by signal decomposition methods such as variational mode decomposition (VMD) [89], empirical mode decomposition (EMD) [90], empirical wavelet transform (EWT) [91] and so on.
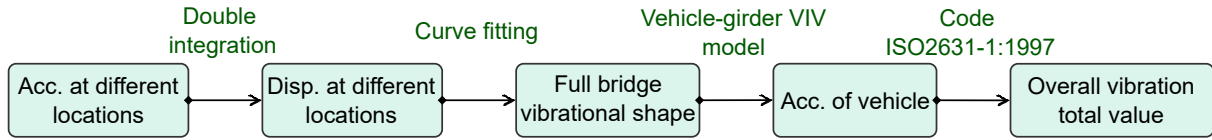
Figure 6: Process of driving comfort evaluation based on vibration level.

2.4. VIV driving evaluation

When the main girder of a bridge experiences VIVs (here, we consider vertical VIV), the vibration acceleration and displacement significantly increase, thus producing unfavorable effects on vehicles passing on the bridge deck. On the one hand, large-magnitude acceleration will affect driving comfort [92, 93, 23]. On the other hand, the rise and fall of the bridge deck can interfere with the driver's sight [48, 22]. Real-time assessment of these two aspects can assist in formulating traffic control schema during VIV.

2.4.1. Driving comfort based on vibration level

The process of assessing driving comfort based on the vibration level is illustrated in Figure 6: (a) integrating the acceleration at each measurement point on the main girder twice to obtain the dynamic displacement, (b) fitting the vibration shape of the entire bridge using dynamic displacements at measured points at any given time, (c) calculating the vibration acceleration of the vehicle during bridge crossing using the vehicle-girder VIV model, (d) evaluating driving comfort by calculating the overall vibration total value (OVTV) according to related codes. Step (a) has been described in Section 2.2.1, and the following sections will explain the remaining three.

Fitting vibration shape of the main girder. Express the vibration shape (dynamic configuration) $y_g(x; t)$ of the main girder at time t as a superposition of several shape functions:

$$y_g(x; t) = \sum_{k=1}^{K} w_k(t) \phi_k(x, \theta_k(t)). \quad (15)$$

Here, $\phi_k(x, \theta_k(t))$ represents the shape function, $\theta_k(t)$ denotes the parameters of the shape function, and $w_k(t)$ represents the weight of the shape function. The form of the shape function is determined, while the weights and parameters vary with time. The problem of fitting the dynamic configuration is to determine the weights and parameters of shape functions based on measured data.

For any given time t, considering the dynamic displacements $\{d_i(t)\}$ at C measurement points on the main girder as target values, and the weights $w_k(t)$ and parameters $\theta_k(t)$ of the shape functions as unknown variables, the following optimization problem can be formulated:

$$\{w_k(t), \theta_k(t)\} = \arg \min_{\{w_k(t), \theta_k(t)\}} \sum_{i=1}^{C} \left(y_g(d_i(t); t) - d_i(t) \right)^2. \quad (16)$$

The above equation can generally be solved using LSM. In this paper, we employ the implementation by `fit` function in MATLAB [94] to fit the relevant parameters.

Vehicle-girder VIV model. As shown in Figure 7, the moving vehicle is simplified to a system as a moving-wheel-mass (M_2) + spring (k_1) and damper c_1 + mass-on-spring (M_1). Denote the deflection of the girder at time t as $y_g(x; t)$ and the dynamic displacement of M_1 as $y_v(t)$. Assuming the mass under spring M_1 moves along the span of the girder without separating from the contact surface, its displacement is consistent with the deflection of the girder. Then the dynamic equilibrium equation of M_2 is given as follows:

$$M_1 \ddot{y}_v(t) + c_1 \left(\dot{y}_v(t) - \frac{\partial y_g(vt, t)}{\partial t} \right) \\ + k_1 \left(y_v(t) - y_g(vt; t) \right) = 0, \quad (17)$$

where the dynamic configuration of girder $y_g(x; t)$ at each time instant is obtained by fitting measured data, so it is known. Since y_v and y_g are discretized in time, the derivatives that appeared in the above equation are calculated using the difference method. Given the initial conditions, the vibration response of the vehicle at each instant can be calculated step by step.

Overall vibration total value (OVTV). In this paper, we use OVTV based on whole-body vibration measurements to assess driving comfort. OVTV is a criterion recommended in the code ISO 2631-1 [95], which has also been utilized in other related works [92, 93, 23].
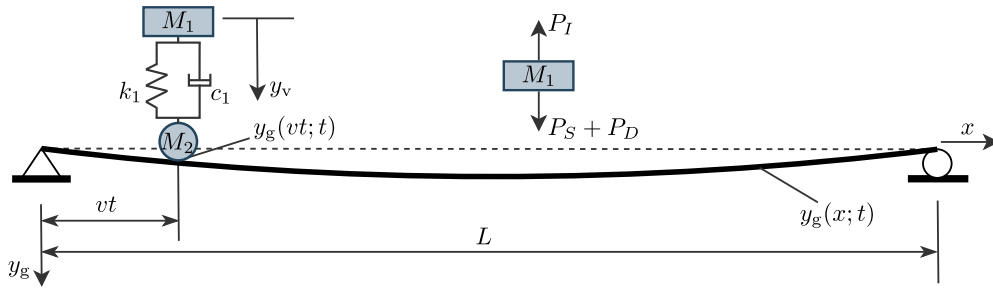
Figure 7: Vehicle-girder VIV model.

The whole-body vibration measurement considers all vibrations transmitted to the human body through supporting surfaces. For a seated passenger, there are three supporting surfaces: seat, backrest, and floor, and each is considered with respect to three translation directions: vertical, lateral, and front-back, along with three overall rotation directions: pitching, rolling, and yawing, resulting in a total of 12 degrees of freedoms (DOFs). Among them, the front-back and yawing responses have small contributions that are usually ignored [92]. The responses at the remaining 8 DOFs can be calculated from the motion of the vehicle centroid (M_1) as follows:

$$a_{vs} = a_{vb} = a_{vf} = \ddot{Z}_v, \tag{18a}$$

$$a_{ls} = a_{lb} = a_{lf} = \ddot{Y}_v, \tag{18b}$$

$$a_{ps} = \ddot{\theta}_v \cdot d_s, \tag{18c}$$

$$a_{rs} = \ddot{\varphi}_v \cdot y_s + \frac{1}{2}\ddot{\varphi}_v \cdot h_s, \tag{18d}$$

where a_{ij} denotes the vehicle acceleration in different DOF: subscript $i(= v, l, p, r)$ represents the response direction where v, l, p, and r represent vertical, lateral, pitching, and rolling directions; subscript $j(= s, b, f)$ denotes the response axis location where s, b, and f represent seat, backrest, and floor; $\ddot{Z}_v, \ddot{Y}_v, \ddot{\theta}_v$ and $\ddot{\varphi}_v$ represent vertical, lateral, pitching, and rolling accelerations at the vehicle centroid; d_s, y_s, and h_s represent the distance between the seat and the vehicle centroid in longitudinal, transverse, and vertical directions.

According to the standard ISO 2631-1 [95], the vibration response in every direction should be frequency-weighted to consider the differences in the impact of vibration at different frequencies on the human body. The specific procedures are transferring the raw response into the frequency domain by Fourier transform, multiplying it by the frequency weighting factor, and then using the inverse Fourier transform to convert the weighted spectrum back to the time domain. The recommended values for the frequency

Table 3
Comfort criteria based on OVTV values.

OVTV value (m/s^2)	Comfort level
< 0.315	Not uncomfortable
0.315 ~ 0.63	A little uncomfortable
0.5 ~ 1	Fairly uncomfortable
0.8 ~ 1.6	Uncomfortable
1.25 ~ 2.5	Very uncomfortable
> 2.0	Extremely uncomfortable

weighting factors can be obtained from ISO 2631-1 [95].

OVTV [95] is a comprehensive evaluation criterion that considers the vibration effects from different axes/directions. It is calculated based on the RMS values of all frequency-weighted responses transmitted to the human body:

$$\text{OVTV} = \sqrt{\begin{array}{l} M_k^2\text{RMS}_{vs}^2 + M_d^2\text{RMS}_{ls}^2 + M_e^2\text{RMS}_{ps}^2 \\ +M_e^2\text{RMS}_{rs}^2 + M_c^2\text{RMS}_{vb}^2 + M_d^2\text{RMS}_{lb}^2 \\ +M_k^2\text{RMS}_{vf}^2 + M_k^2\text{RMS}_{lf}^2 \end{array}}. \tag{19}$$

Here, RMS_{ij} denotes the RMS of acceleration a_{ij} after frequency weighting; and $M_i(i = k, d, e, c)$ is multiplying factor for different DOF direction, M_i in the equation is taken as $M_k = 1.00, M_d = 1.00, M_e = 0.40, M_e = 0.20, M_c = 0.40, M_d = 0.50, M_k = 0.40, M_k = 0.25$ in turns.

To facilitate the assessment of driving comfort, ISO2631-1 [95] divides six comfortable levels according to the range of values of OVTV, as shown in Table 3.

Unlike under laboratory or numerical conditions, it is difficult to obtain the vibration response of an actual moving vehicle in all eight directions mentioned above through the bridge monitoring system. Moreover, for bridges during VIV, the magnitude of the vertical acceleration is much higher than that in other directions.
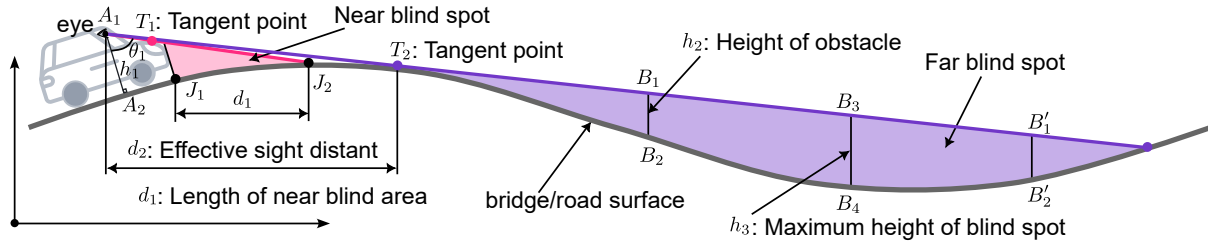
Figure 8: Illustration of near/far blind spot, effective sight distance, and maximum height of far blind spot.

Therefore, we only considered the vertical acceleration of the vehicle $\ddot{Z}_v$ (calculated by Equation 17). Then, the above Equation 19 can be simplified as

$$\text{OVTV} = \sqrt{M_k^2 \text{RMS}_{vs}^2 + M_c^2 \text{RMS}_{vb}^2 + M_k^2 \text{RMS}_{vf}^2}. \tag{20}$$

2.4.2. Driving safety based on field of view

The vehicle blind spot refers to the area formed due to the obstruction of the driver's line of sight. As there may be obstacles, pedestrians, or vehicles in the blind area, it is easy to cause driver's misjudgment and misoperation, thus causing traffic accidents. This section evaluates driving safety under VIV by identifying the time-varying near and far blind spots.

As shown in Figure 8, the near blind spot refers to the invisible area caused by the obstruction of the front part of the vehicle. Its length is the horizontal distance between the front-most point J_1 of the vehicle and the intersection J_2 of the line of sight ($A_1 T_1$) and the girder's configuration. The far blind spot refers to the invisible area caused by the undulating bridge deck obstructing the driver's line of sight ($A_1 T_2$), resulting in a discontinuous field of view. Assuming obstacles have a certain height denoted as h_2, all obstacles lower than h_2 within the interval from B_2 to B_2' are not visible. Denote the maximum height of far blind spot as h_3, i.e., obstacles higher than h_3 are visible. The horizontal distance between the driver's location A_2 and the tangent point T_2 is called effective sight distance. The following will describe the identification of the length of near blind spot, effective sight distance, and maximum height of far blind spot.

Identification of the length of near blind spot. As shown in Figure 9(a), assume that the vehicle is traveling at a constant speed v and is located at the point A_2 on the bridge deck at the moment t, whose coordinates can be expressed as $(x_v, y_v) = (vt, y_g(vt; t))$; the driver's eye height is h_1 and his eyes are located at

A_1 point, the coordinates of A_1 can be expressed as $(x_e, y_e) = (x_v - h_1 \sin(\alpha), y_v + h_1 \cos(\alpha))$, α is the angle between the tangent line of the bridge at the point A_1 and the horizontal line; the tangent point of the driver's line of sight to the hood of the car is T_1; in the case where the eye height h_1 is known, the angle θ_1 between the lines $A_1 T_1$ and $A_1 A_2$ is also known, from which the equation of the line of sight, $y_s(x; t)$, corresponding to the near blind spot can be obtained. Associating the main beam configuration expression, $y_g(x, t)$, the intersection point J_2 in the figure can be found as follows:

$$\begin{cases} y_s(x; t) = \tan(\theta_1 + \alpha)(x - x_e) + y_e, \\ y_g(x; t) = \sum_{k=1}^{K} w_k(t) \phi_k(x; \theta_k(t)). \end{cases} \tag{21}$$

Further, the length of the near blind spot is:

$$d_1 = x_{J_2} - x_v - l_1 \cos(\alpha), \tag{22}$$

where l_1 is the vertical distance from the eye to the foremost plane of the vehicle as shown in Figure 9(a).

Identification of effective sight distance and maximum height of far blind spot. As shown in Figure 9(b), assuming that the line of sight is tangent to the bridge deck at the nearest T_2, the slope of $A_1 T_2$ is equal to that of the tangent of the girder configuration at T_2:

$$k = \frac{y_e - y_{T_2}}{x_e - x_{T_2}} = \left. \frac{\partial y_g(x; t)}{\partial x} \right|_{x = x_{T_2}}. \tag{23}$$

Thus the coordinate of $T_2 = (x_{T_2}, y_{T_2})$ can be solved.

It is unavailable to solve the above equation analytically and is generally solved by a root-finding algorithm, which is figured out in this paper using `fzero` function in MATLAB [96]. Then, the line of sight equation $y_s(x; t)$, effective sight distance d_2, and maximum height of far blind spot h_3 can be expressed as follows, respectively:

$$y_s(x; t) = k(x - x_{T_2}) + y_{T_2}, \tag{24}$$
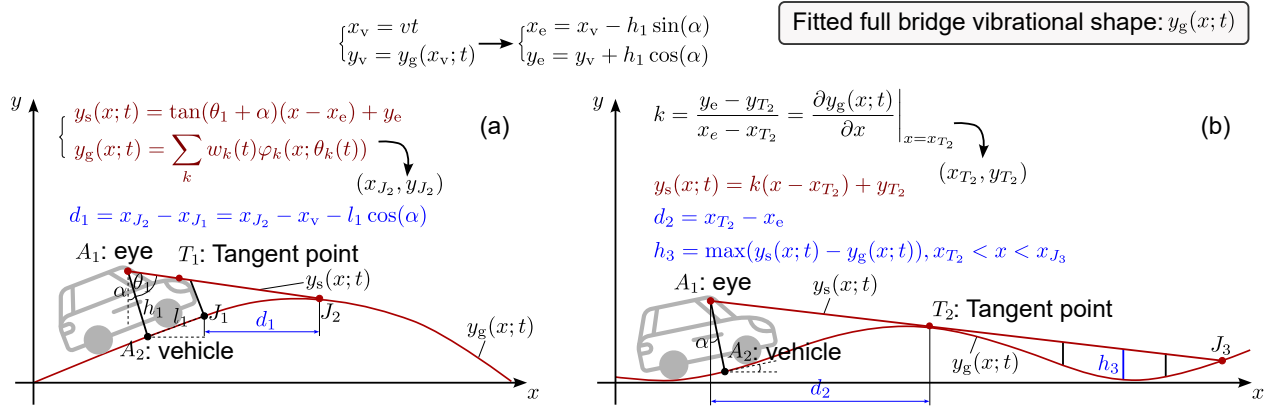
Figure 9: Identification of the length of near blind spot, effective sight distance, and maximum height of far blind spot.

$$d_2 = x_{T_2} - x_e, \tag{25}$$

$$h_3 = \max(y_s(x;t) - y_g(x;t)), \ x_{T_2} < x < x_{J_3}. \tag{26}$$

2.5. VIV advanced prediction

The two VIV prediction tasks are considered: first, predicting whether VIV will occur (before moment D in Figure 2(a)); second, predicting the stable amplitude that VIV can reach (before moment E in Figure 2(a). To accomplish these, we first establish three models offline: a statistical model to summarize the rules of wind speed and direction corresponding to VIV events, a neural network model to predict the value of the VIV index, and a dynamical model to calculate the stable amplitude VIV can reach. Then, online prediction is performed following the logic shown in Figure 10: (1) the statistical model determines if the ambient wind field is conducive to VIV happiness; (2) If so, the neural network model is used to predict VIV index. (3) If the predicted VIV index exceeds a certain threshold, the dynamical model is employed to calculate the stable amplitude VIV can achieve, and a VIV warning signal is sent. Note that when predicting the VIV index and calculating the stable amplitude, the results of VIV identification and tracking are also utilized, which are not depicted in the figure.

The statistical model primarily provides the ranges of locked wind speed and wind direction when VIV occurs, denoted as $[v_{\text{VIV}}]$ and $[\theta_{\text{VIV}}]$, which can be obtained from historical wind speed data of VIV events.

2.5.1. VIV occurrence prediction based on neural network

Using the VIV identification algorithm proposed in Section 2.2 allows us to determine the starting and
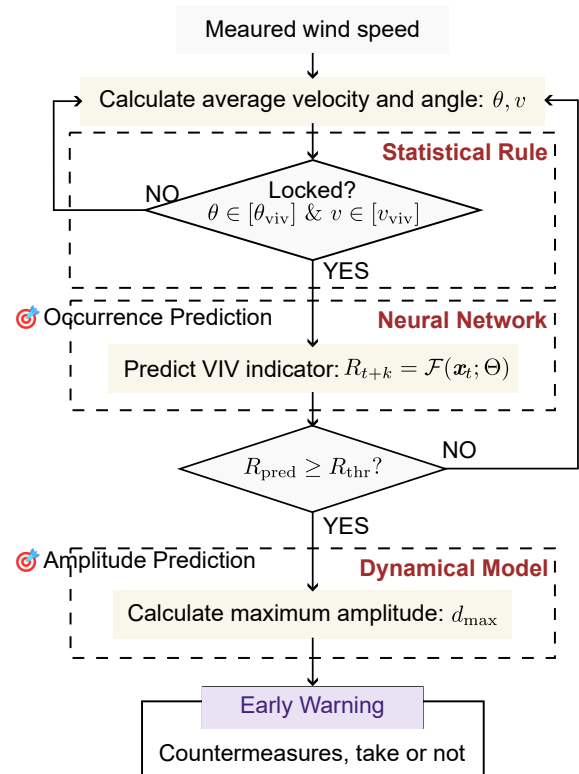
Figure 10: The process of VIV prediction.

ending of VIV events from historical acceleration data and then intercept wind speed and acceleration belonging to the corresponding VIV event. As illustrated in Figure 11, the VIV datasets for training the neural network are constructed as follows: (a) For each VIV event, the raw data is divided into sub-segments of length T, and the overlap length between sub-segments is $T - \Delta T$; (b) Calculate the features corresponding to each sub-segment, including average wind speed v,
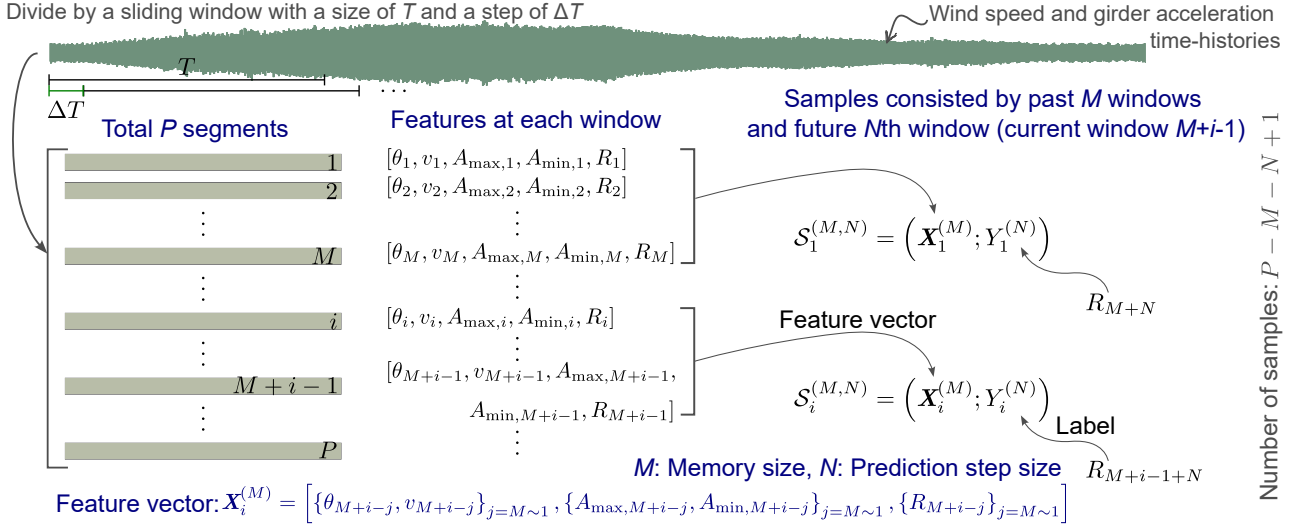
Figure 11: Construction of VIV datasets: For each VIV event, the original data is divided into sub-segments using a sliding window with a length of T and an overlap of $T - \Delta T$. The sub-segments are then used to construct VIV samples.

average wind direction θ, maximum amplitude $A_{\max}$, minimum amplitude $A_{\min}$, and vortex index R; (c) A VIV sample $S_i^{(M,N)} = \left(X_i^{(M)}, Y_i^{(N)} \right)$ is expressed as:

$$\left(X_i^{(M)}, Y_i^{(N)} \right) = \left(\left[\left\{ \theta_{M+i-j}, v_{M+i-j} \right\}_{j=M\sim1}, \right.\right.$$
$$\left\{ A_{\max,M+i-j}, A_{\min,M+i-j} \right\}_{j=M\sim1}, \quad (27)$$
$$\left. \left\{ R_{M+i-j} \right\}_{j=M\sim1} \right], R_{M+i-1+N} \right),$$

where i is the index of the sample; $M + i - j$ is the index of the sub-segment, i.e., θ_{M+i-j} denotes the average wind direction calculated from the $(M+i-j)$th segment; M is the historical memory length; N is the prediction step; $X_i^{(M)}$ denotes the feature vector composed of feature values corresponding to M historical segments; $Y_i^{(N)}$ denotes the VIV index corresponding to the Nth segment in the future. Assuming that the lth VIV event is divided into P_l data sub-segments, the number of samples formed by this VIV event is $S_l = P_l - M - N + 1$. The sample sets from all VIV events are pooled together to form the historical VIV datasets as:

$$\mathcal{D} := \left\{ \left(X_i, Y_i \right) \right\}_{i=1}^{\sum_l S_l}. \quad (28)$$

We utilize the SDE-Net neural network [97] to establish the mapping from the historical feature vector $X_i^{(M)}$ to the future VIV index value $Y_i^{(N)} := R_{M+i-1+N}$, $\mathcal{F} : x_t \rightarrow R_{t+k}$. The advantage of this network (Figure 12) is that it gives the DNN the ability to estimate uncertainty. The input feature vector is first passed through a fully connected layer, followed by a stack of SDE-Net layers with shared parameters. Finally, the prediction of the VIV index and its variance are output through another fully connected layer. The SDE-Net layer contains two sub-layers: a drift layer and a diffusion layer. The drift layer is a fully connected layer with a ReLU activation function. The input to the diffusion layer undergoes a fully connected layer with a ReLU activation function, followed by another fully connected layer with a Sigmoid activation function, producing a diffusion term. This diffusion term is multiplied by a standard Gaussian process to simulate the cognitive uncertainty.

Assume the input to the kth SDE-Net layer is h_k, and the output is h_{k+1}, then we have:

$$h_{k+1} = h_k + f(h_k; \theta_f) + g(h_k; \theta_g)z_k, z_k \sim \mathcal{N}(0,1). \quad (29)$$

The above equation can be viewed as a discrete form of the stochastic differential equation (SDE):

$$dh_t = f(h_t, t; \theta_f)dt + g(h_t, t; \theta_g)dW_t, \quad (30)$$

where W_t is the standard Brownian motion. By introducing residual connections and the diffusion term, the network architecture is equivalent to a differential equation dynamical system, which provides a non-Bayesian approach for quantifying uncertainty. Moreover, the diffusion term can be regarded as a kind of regularization of the neural network, which can improve the robustness of network learning.
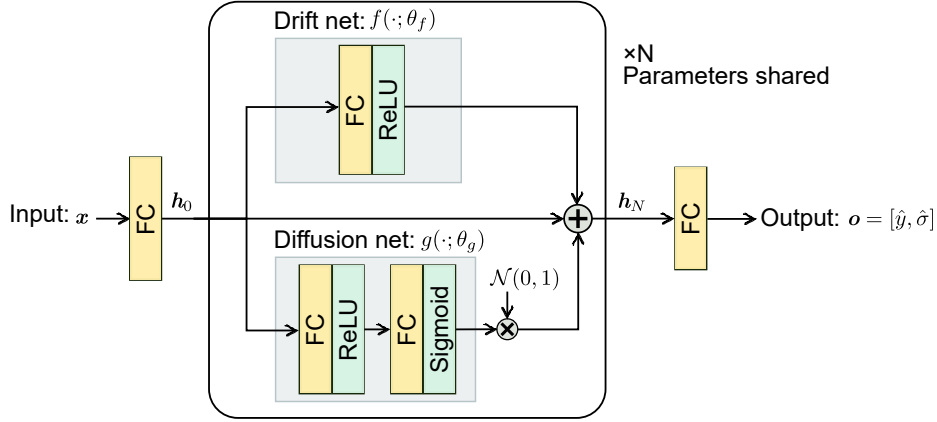
Figure 12: Architecture of the neural network for VIV index prediction.

The network adopts a strategy of alternating optimization between the drift net and the diffusion net. The loss function used for drift net is:

$$\mathcal{L}_f = \min \mathbb{E}_{x \sim P_{\text{train}}} \mathcal{L}(o) = \frac{1}{N} \sum_{i=1}^{N} \frac{(\hat{y}_i - y_i)^2}{\hat{\sigma}_i^2} + \frac{1}{2} \ln \hat{\sigma}_i^2,$$
(31)

where, $\hat{y}_i$ and $\hat{\sigma}_i$ represent the predicted value and variance for the ith sample, respectively; y_i denotes the true value; and N represents the total number of samples. The term P_{train} refers to the distribution of the training data. The diffusion layer can be regarded as a classifier trained to distinguish between samples within the distribution (labeled as 1) and out-of-distribution (OOD) samples (labeled as 0). The loss function used for this purpose is a cross-entropy function:

$$\mathcal{L}_g = \min \mathbb{E}_{x \sim P_{\text{train}} || P_{\text{OOD}}} \mathcal{L}(g(h_0; \theta_g))$$
$$= -\frac{1}{N} \sum_{i=1}^{N} \log(g_{x_i \sim P_{\text{train}}}(h_0; \theta_g))$$
(32)
$$+ \log(1 - g_{x_i \sim P_{\text{OOD}}}(h_0; \theta_g)).$$

The OOD samples are obtained by adding additive Gaussian noise to the data. During training, the backpropagation is first performed using Equation 31 to update only the parameters of the drift layer as well as the head and tail fully connected layers. Then, the backpropagation is performed using Equation 32 to update only the parameters of the diffusion layer. This alternating process continues until achieving convergence.

The network design described above enables the system to achieve better prediction accuracy for data within the distribution by primarily relying on the drift net. While for OOD data, the system relies on the diffusion net, exhibiting high diffusion characteristics (high variance), thereby assessing the uncertainty of the results.

2.5.2. VIV stable amplitude prediction based on dynamical model

For the bridge's girder experiencing VIV, the vertical motion can be described by an SDOF system as follows:

$$m\ddot{y} + 2m\xi\omega_1\dot{y} + m\omega_1^2 y = F_{\text{VIV}}(t),$$
(33)

where y is the vertical vibration of the main girder; m, ξ, and ω_1 are the mass per unit length, damping ratio, and natural frequency of the structure, respectively.

We employ the widely used Scanlan empirical nonlinear model [29] to describe the right-end force term $F_{\text{VIV}}(t)$:

$$F_{\text{VIV}} = \frac{1}{2}\rho U^2 (2D) \left[Y_1(K) \left(1 - \varepsilon \frac{y^2}{D^2} \right) \frac{\dot{y}}{U} \right.$$
$$\left. + Y_2(K)\frac{y}{D} + \frac{1}{2}C_L(K)\sin(\omega t + \theta) \right].$$
(34)

In the equation above, ρ denotes the air density; U represents the incoming wind velocity; D corresponds to the characteristic width of the section; $K = \omega D/U$ is the reduced frequency, where ω is the vortex shedding frequency; ε, $Y_1(K)$, $Y_2(K)$, and $C_L(K)$ are aerodynamic parameters that need to be determined, typically through wind tunnel tests.

According to the study of Ehsan and Scanlan [29], the aerodynamic lift term $\frac{1}{2}C_L(K)\sin(\omega t + \theta)$ due to vortex shedding during VIV can be neglected. Furthermore, the study also found that there are no significant

changes in the structural natural frequency between lock-in and regular condition [50], which means that the aerodynamic stiffness term $Y_2\frac{y}{D}$ in the model can be further neglected. Therefore, the dynamical model can be simplified as follows:

$$F_{\text{VIV}} = \frac{1}{2}\rho U^2(2D)Y_1\left(1-\varepsilon\frac{y^2}{D^2}\right)\frac{\dot{y}}{U}. \qquad (35)$$

Combining the Equations 8 and 35, the simplified VIF model is a Van der Pol oscillator with the dimensionless form of

$$\ddot{\eta}(s)+2\xi K_1\dot{\eta}(s)-m_rY_1(K)(1-\varepsilon\eta^2(s))\dot{\eta}(s)+K_1^2\eta(s) = 0, \qquad (36)$$

where $\eta = y/D$ is the dimensionless displacement; $m_r = \rho D^2/m$ is the mass ratio; $K_1 = \omega_1 D/U$ is the reduced frequency; and $s = Ut/D$ is the dimensionless time. Due to frequency locking, the vortex shedding frequency and the structural frequency are considered equal, i.e., $\omega_1 = \omega, K_1 = K$. Then the solution of Equation 36 can be expressed as:

$$\eta(s) = A(s)\cos(Ks - \varphi_0), \qquad (37a)$$

$$A(s) = \frac{\beta}{\sqrt{1-\left(\frac{A_0^2-\beta^2}{A_0^2}\right)e^{-(\alpha\beta^2/4)s}}}, \qquad (37b)$$

where A_0 is the initial amplitude of the system; φ_0 is the initial phase at $s = 0$; and $A(s)$ is a slowly varying amplitude, where the parameters α and β are defined as:

$$\alpha = m_rY_1\varepsilon, \qquad (38a)$$

$$\beta = \frac{2}{\varepsilon}\sqrt{1-\frac{2\xi K}{m_rY_1}}. \qquad (38b)$$

From Equation 37(b), it is known that when $s \to +\infty$, the stable amplitude $A_{+\infty} = \beta$. In the monitoring environment, β can be determined from the time history of the VIV response.

Given the appearance of a stable limit cycle during VIV, the system aerodynamic input energy and the structural damping dissipation energy are equal:

$$\int_t^{t+T}\left(2m\xi\omega_1 - \rho U DY_1\left(1-\varepsilon\frac{y^2}{D^2}\right)\right)\dot{y}^2dt = 0, \qquad (39)$$

where T is a vibration period.

Combining the expression for the vibration response in Equation 37(a), the stable amplitude during VIV can be obtained as

$$y_0 = \left(\frac{\rho U D^2Y_1 - 2m\xi\omega_1 D}{\rho U DY_1\varepsilon}\right)^{1/2}. \qquad (40)$$

Based on Equation 40, once the damping ratio ξ, natural frequency ω_1, wind speed U, and aerodynamic parameters Y_1 and ε are determined, the stable amplitude of VIV can be calculated. Among them, the structural natural frequency ω_1 can be obtained from the measured vibration data. The structural damping ξ can be obtained from the historical non-VIV data. The wind speed U can be taken as the average value of the measured wind speed during VIV. The aerodynamic parameters Y_1 and ε are dependent on the wind speed and the order of VIV and can be got through historical VIV data. The specific steps are as follows:

1. For a given VIV event, determine the vibration order and the average wind speed in the VIV development period;

2. Determine the stable amplitude β;

3. Calculate the amplitude envelope $A(s)$ in VIV development period, and fit the value of α according to Equation 37(b) using the following equation:

$$\ln\left(\frac{A_0^2(A(s)^2 - \beta^2)}{A^2(s)(A_0^2 - \beta^2)}\right) = -\frac{\alpha\beta^2}{4}s; \qquad (41)$$

4. Compute the aerodynamic parameters Y_1 and ε corresponding to this VIV event by Equation 38;

5. Repeat steps 1~4 to obtain the relationship between the aerodynamic parameters Y_1 and ε with wind speed and vibration order to form a parameters table.

Once the occurrence of VIV is predicted or identified, the corresponding aerodynamic parameters Y_1 and ε can be obtained from the parameters table based on the current order and the measured wind speed. Then the stable amplitude of VIV can be calculated using Equation 40. At the same time, update the table of aerodynamic parameters.

3. Case analysis and system implementation

This section will present the application of the proposed methods on two long-span suspension bridges.
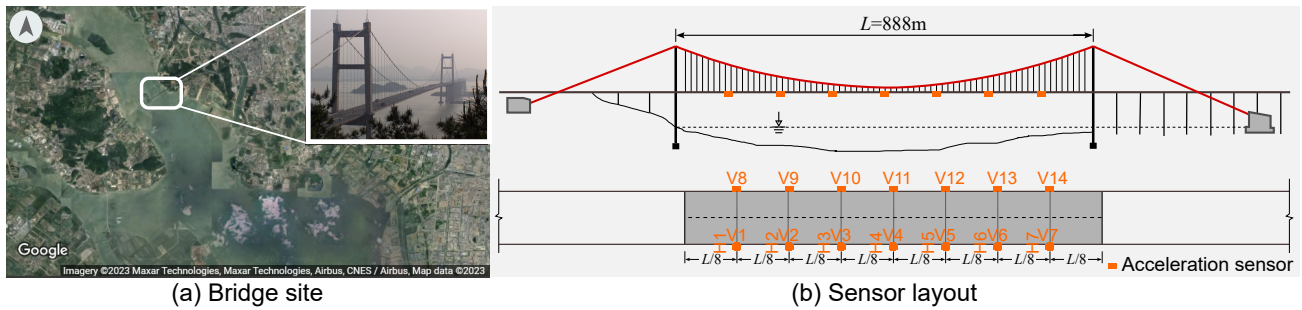
Figure 13: The site and sensor layout of Humen Bridge.

Firstly, a brief overview of the engineering backgrounds of the two bridges will be provided. Then, the effectiveness of the proposed methods will be validated using VIV data from the two bridges. Finally, the implementation details of a VIV monitoring system constructed for one of the bridges will be introduced.

3.1. Background of structure
3.1.1. Humen Bridge
Humen Bridge, located in the coastal region of southern China (Figure 13(a)), is a double-tower single-span suspension bridge with a span of 888 m. The bridge has two-way six lanes, designed speed is 120 km/h. It was completed and opened to traffic in June 1997. On the afternoon of May 5, 2020, Humen Bridge experienced abnormal oscillations, leading to a full traffic closure. Subsequent investigations revealed that the main reason for the bridge's abnormal vibration was due to the temporary setting of water horses along both sides of the bridge, which changed the aerodynamic shape of the steel box girder and triggered VIV under specific wind conditions [3, 2]. A monitoring system was installed on the bridge to understand the structural vibration. As shown in Figure 13(b), seven vertical acceleration sensors were evenly arranged on the upstream and downstream sides of the main span, respectively. And seven lateral acceleration sensors were installed near the vertical acceleration sensors on the upstream side. Refer to the figure for the sensor's number. All sensors are synchronized and sample at a frequency of 50 Hz.

3.1.2. Xihoumen Bridge
Xihoumen Bridge, located in the coastal region of eastern China (Figure 14(a)), is a double-tower double-span suspension bridge with a span of 1650 m + 578 m. The bridge has two-way four lanes, designed speed is 80 km/h. It was opened to traffic in 2009. The bridge adopts a split steel box girder with a width of 36 m

and a height of 3.26 m, and the spacing between the left and right sides is 6 m. The designation of split steel box girder offers excellent flutter stability [98]. But it also facilitates the reattachment of vortices at the tail of the downstream beam when crosswind passes through, which can lead to VIV [9]. The Xihoumen Bridge has established a comprehensive SHM system, which includes structural responses such as multi-directional acceleration, strain, and displacement of the main girder, as well as environmental variables such as temperature, humidity, and wind speed. The arrangement of some sensors is shown in Figure 14(b). Vertical acceleration sensors were installed at the $1/4L$, $1/2L$, and $3/4L$ on the upstream and downstream sides of the main span and $1/2L'$ on the upstream and downstream sides of the side span. Six three-axis anemometers were placed near the acceleration sensors on the main span and 6m above the girder surface. Two propeller anemometers were placed on the top of the two towers. Refer to the figure for the sensors' number. All sensors are synchronized, and the acceleration sensors and anemometers sample at a frequency of 50 Hz and 10 Hz, respectively.

3.2. Case analysis
3.2.1. VIV identification, tracking, and evaluation results
On June 16, 2020, the Humen Bridge experienced a VIV event. In the following, we utilize the monitoring data from that day to analyze the effectiveness of the proposed methods for VIV identification, tracking, and evaluation.

VIV index. Figures 15(a) and 15(b) plot the original acceleration time history and the integrated displacement time history at the sensor V3 (Figure 13(b)). In terms of instantaneous magnitude, the acceleration under normal vibration conditions also reaches the level of VIV. However, in the integrated displacement signal,

(a) Bridge site (b) Sensor layout
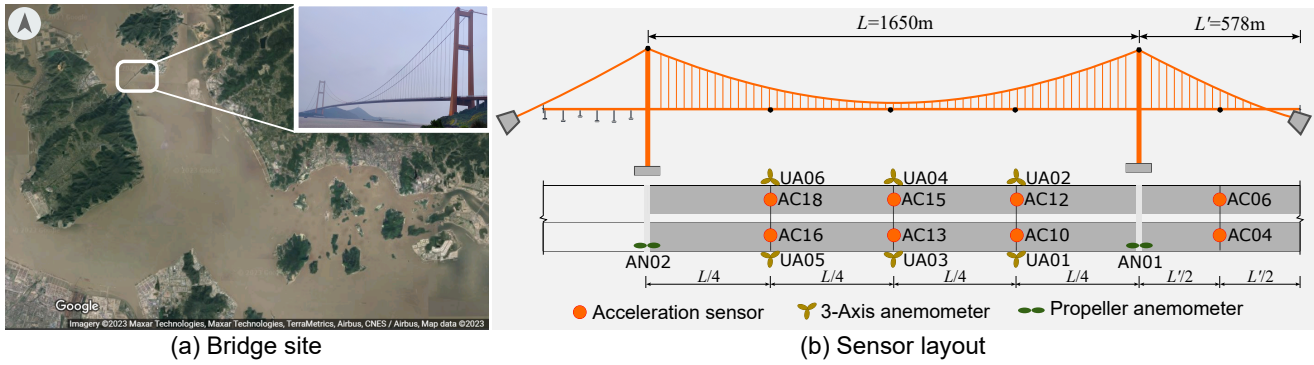
Figure 14: The site and sensor layout of Xihoumen Bridge.

the vibration level during the VIV significantly exceeds that of other periods. Because during the integration process, the signal undergoes filtering, and some high-frequency components are removed. Figures 15(c) and 15(d) shows the spectrum of the raw acceleration and the visualization of R index on the complex plane corresponding to a VIV time. And Figures 15(e) and 15(f) show that corresponding to a non-VIV time. It can be seen, due to the single-mode nature of VIV, the trajectory of the analytic signal during VIV is confined within a narrower circular envelope on the complex plane, whereas during non-VIV, it tends to spread over the whole circular region. Figure 15(g) gives the variation of the R index over a 10-hour period. It is observed that the value of R during VIV is significantly higher than the value during the regular vibration before and after, and its magnitude can reflect the degree of VIV development. By setting an appropriate threshold (set to 0.1 in the figure), it is possible to judge the occurrence of VIV. Here R index is calculated directly using the analytic signal of the acceleration after removing the trend term and low-pass filtering with a cutoff frequency of 15 Hz, while not calculated using the integrated dynamic displacement. Because experimental results indicate that although the index calculated from displacement exhibits larger values during VIV compared to the index calculated from the acceleration, it also has relatively large values during non-VIV, making it difficult to distinguish between the two different vibration cases. This is because the operations of cumulative summation, baseline correction, and drift removal involved in displacement integration will remove noise terms and some non-dominant components, causing the integrated displacement close to an SDOF signal.

Amplitude, phase, frequency, and modal shape during VIV. Set the threshold of the VIV index as 0.01. and When $R > 0.01$, the corresponding amplitude, phase, frequency, and modal shape can be calculated using Equations 10, 11, 12, and 13, respectively. The results are exhibited in (Figures 16 and 17). The displacement amplitude provides a visual indication of the magnitude of the vibration level, and the maximum displacement of this VIV event at V3 ($3/8L$) is about 4 cm. The frequency during the VIV is not constant. In this case, the locking frequency has a fluctuation of about 0.002 Hz throughout the VIV event. With the development of the VIV process, the change of frequency shows a certain pattern, that is, in the beginning, the frequency is higher and exhibits more fluctuates; with VIV reaches the steady state, the frequency becomes stable; at the end of VIV, the frequency starts to produce large fluctuations again. This could be attributed to a more intense and unstable interaction between the flow field and the structure during the development and decaying periods of VIV.

Figure 17 depicts the varying vibration shape (at this time, reduced to modal shape) obtained from the displacement measurements at distributed points along one side of the girder. The time interval is 2 minutes in the figure. In this particular VIV event, the bridge vibrates in the 3rd order mode. Note that the deflection curve of the bridge is not completely symmetrical about the mid-span position, with a slight lag observed on the left side. By incorporating the prior knowledge of structural dynamics and selecting appropriate shape functions, it is possible to fit a continuous and real-time dynamic configuration of the entire bridge using the displacements at all sensors as control points. This enables the bridge manager to intuitively grasp the vibration state of the bridge and take corresponding measures.
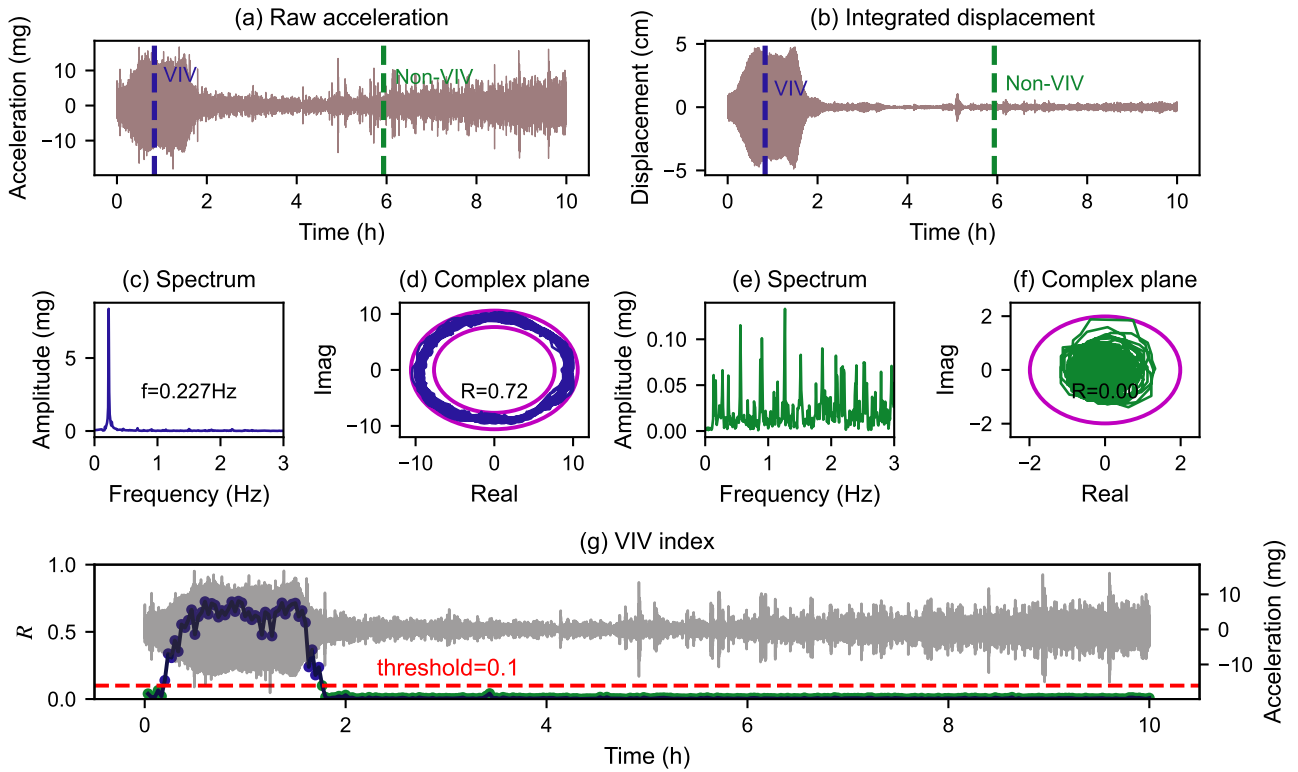
Figure 15: VIV index identification of Humen Bridge on 16 June, 2020.
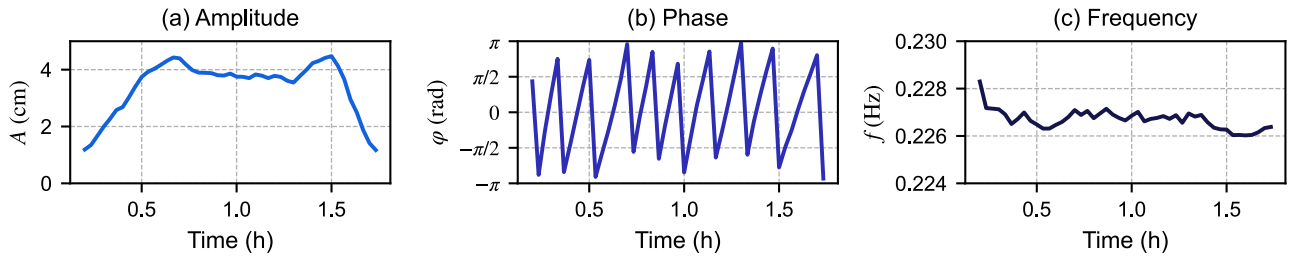
Figure 16: Tracking of amplitude, phase, and frequency during VIV.
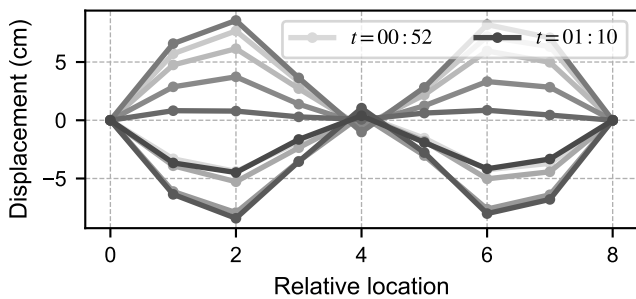
Figure 17: Tracking of vibration/modal shape during VIV.

Representative damping during VIV. We analyzed the variations of representative damping ratios during VIV

of a total of seven sensors, V1~V7 in Figure 13(b), and Figure 18 plots the results. The representative damping ratios exhibit similar varying trends across different positions, albeit with some numerical differences, indicating the non-uniformity in spatial distribution. During this VIV period, the minimum and maximum values of the representative damping are -0.128% and 0.166%, respectively. In the VIV development stage, the negative aerodynamic damping exceeds the structural damping, resulting in a negative damping in total, which leads to an increase in structural amplitude due to net energy input. In the stable stage of VIV, the total damping approaches zero, signifying a balanced energy input-output, resulting in a stable amplitude. In
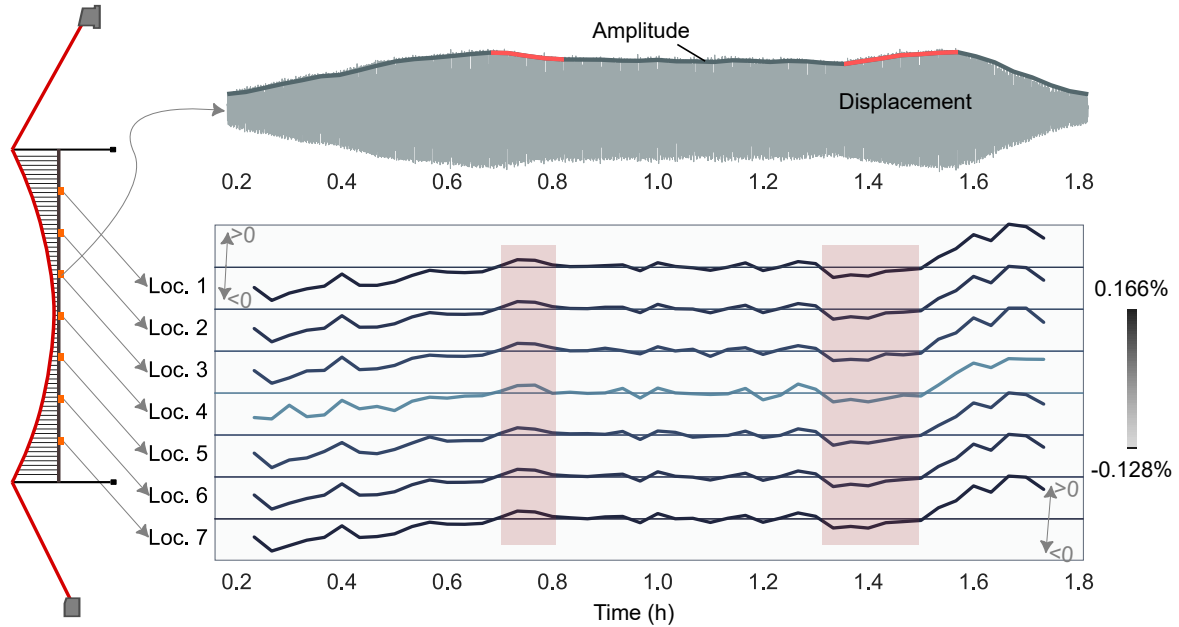
Figure 18: Tracking of representative damping ratio during VIV (shadow corresponds to "peak-and-fall").

the VIV decaying stage, the total damping becomes positive, indicating structural damping reoccupies the dominant position, the energy dissipates, and the structural amplitude gradually decreases. Notably, a "peak-and-fall" phenomenon is observed when the damping transfers from positive to zero or from zero to negative. During the stable stage, the representative damping is fluctuated around zero (correspondingly, the amplitude fluctuates around a certain value), suggesting that the actual fluid-structure coupling system will deviate from the desired value to a certain extent due to the non-stationarity. But it is not enough to break the current equilibrium state. The dynamic balance of this mutual game also reflects in frequency variations in Figure 16(c).

Driving comfort evaluation during VIV. As shown in Figures 19(a) and 19(b), considering a sedan traveling at a speed of 120 km/h passing over an undulating bridge deck that is experiencing VIV (the trajectory of the sedan is the red line in the figure), the variation of the vehicle's vertical acceleration and the analyzed OVTV are shown in Figures 19(c) and 19(d). The parameters of the sedan are listed in the first row of Table 4. The calculation results indicate that when considering only the vertical acceleration caused by VIV according to Equation 20, the frequency-weighted OVTV does not exceed 0.35 m/s^2. And refer to table Table 3, the driving comfort is deemed well. However, according to passenger feedback, driving on the bridge

experiencing VIV can cause obvious discomforts, such as dizziness and nausea. This is partly because the calculation here ignores the input of acceleration from other directions rather than vertical and ignores the influence of the road roughness, resulting in underestimated OVTV values. On the other hand, the impact of bridge deck undulation on passengers' visual perception will exacerbate the physical discomfort, which is currently not considered in the code [95]. The OVTV values are higher during the ascending and descending periods on the bridge, which is related to the triggered VIV mode. As shown in Figure 17, the main girder vibrates in the 3rd order mode, and the displacement around the mid-span is small.

Length of near blind spot during VIV. The variations of the near blind spot for two types of vehicles, sedan and light truck, passing through a bridge experiencing VIV at speeds of 80 km/h, 100 km/h, and 120 km/h, respectively, are depicted in Figure 20. The geometric parameters of the vehicle, including eye height h_1, tangent angle θ_1, and eye-to-car distance d_1, are presented in Table 4. Due to the sedan's lower eye height and larger tangent angle, it exhibits a longer near blind spot length (fluctuating around 5.44 m) than the light truck (fluctuating around 2.137 m). When the two types of cars travel at the same speed on the bridge, the changing laws of the near blind spot keep the same. Comparing the changes in the front blind spot at different speed, it is evident that the effect of vehicle speed is tiny. The
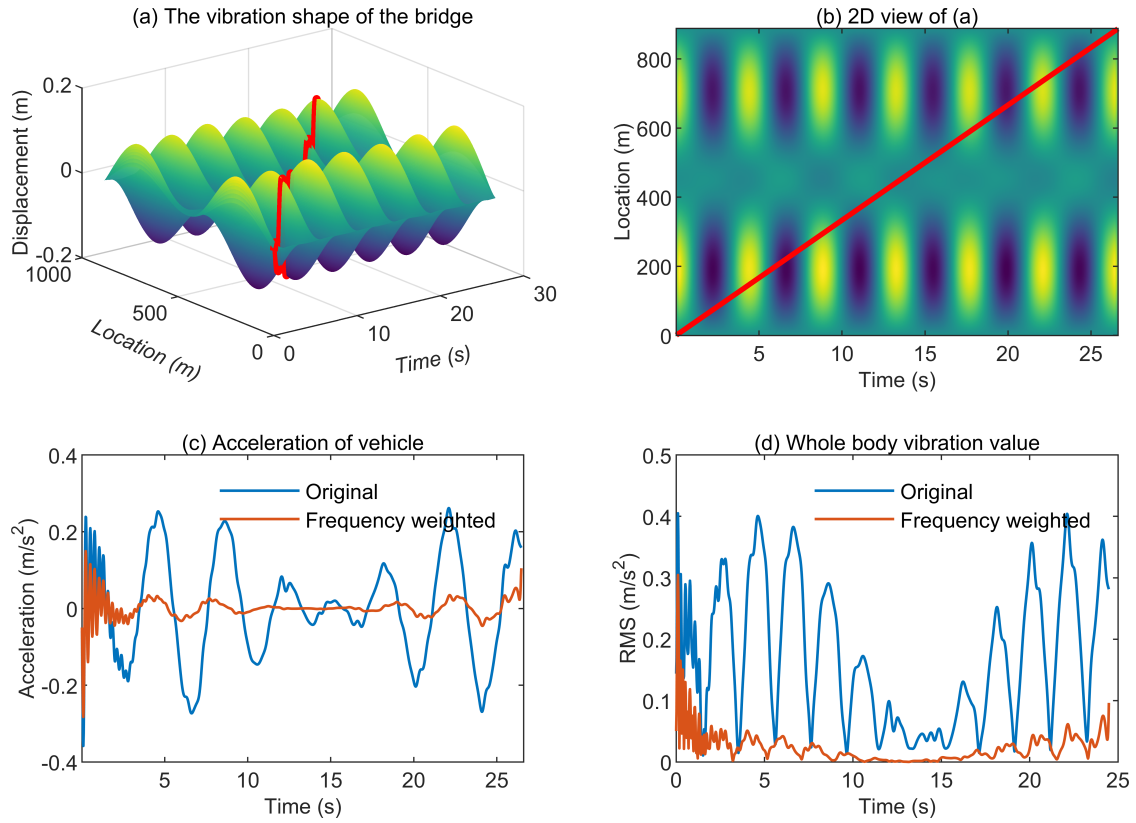
Figure 19: The evaluation of driving comfort during VIV.

Table 4

Parameters of vehicle.

	Mass M_1 (kg)	Vertical stiffness k_1 (kN/m)	Vertical damping c_1 (kN)	Height of eye h_1 (m)	Angle θ_1 (rad)	Eye-to-car distance d_1 (m)
Sedan	1600	436	3.2	1.2	1.42	2.352
Truck	6500	1000	10.0	1.45	1.07	0.763

changes in the near blind spot align with the periodicity of the girder vibrations.

Effective sight distance and maximum height of far blind spot. Similarly, Figures 21 and 22 present the effective sight distance and maximum height of far blind spot over time for a sedan and a light truck, respectively, when passing a bridge experiencing VIV. It should be noted that the effective sight distance and maximum height of far blind spot exist only when the line of sight is obstructed, whereas they are set to zero when the bridge deck has no obstruction to the driver's eye. Due to the lower eye height of the sedan than the light truck, the former exhibits a shorter effective sight distance and a taller maximum height of far blind spot. Additionally, the effective sight distance, maximum height of far blind spot, and their respective locations

on the bridge deck may vary as the bridge configuration changes for vehicles traveling to the same position at different speeds. The discrete-time interval equals the sensor's sampling interval (0.02 s in this case). As the vehicle speed increases, the spatial resolution decreases, resulting in fewer occurrences of far blind spot.

3.2.2. VIV prediction results

The Xihoumen Bridge is chosen as the object of the investigation to validate the VIV prediction methods because this bridge's SHM system has documented a number of VIV events, thereby offering sufficient data samples for building and training the models for prediction.

VIV occurrence prediction We analyzed data recorded by the monitoring system from 2018 to 2021. First,
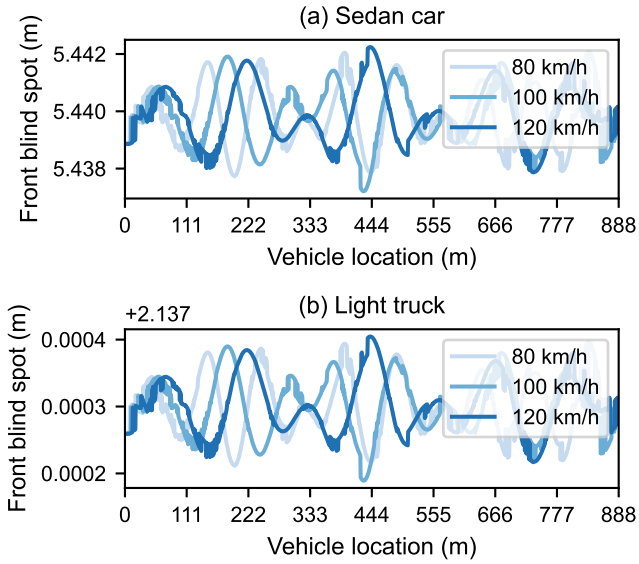
Figure 20: Length of front blind spot during VIV.

Figure 22: Maximum height of far blind spot during a VIV event.

Figure 21: Effective sight distance during a VIV event.

we pick up all the VIV events using the VIV index proposed in Section 2.2, with a threshold set as 0.1, and obtained 67 VIV events. For a singular VIV event, denote the starting and ending times of the period with the VIV index greater than 0.1 as t_1 and t_2, respectively, backtrack for 20 minutes, and select the data from $t_1 - 20$ mins to t_2 as the final data corresponds to this VIV event. Subsequently, we construct VIV samples following the approach presented in Section 2.5.1. The data sub-segment length T is 10 minutes, and the sliding step ΔT is 1 minute. Historical memory

length M is set to 5, and the future prediction step N is taken as 1, 3, 5, 7, and 9, respectively. As a result, datasets with different prediction steps were created. Each contains approximately 13,920 samples. Here, the index and feature values are obtained by averaging the three measurement points on one side of the main span. According to the statistics of the 67 VIV events, the range of wind speeds during VIV is $[v_{\text{VIV}}] = [4, 12]$ m/s, and that of wind directions is $[\theta_{\text{VIV}}] = [30, 60]° \cup [210, 240]°$, which are nearly perpendicular to the bridge axis.

The number of SDE-Net layers in the network is taken as 4. The network is trained using the mini-batch gradient descent method with a batch size of 16. The training process involves 400 epochs, and the learning rate is 0.0001. Figure 23 shows the convergence of the training loss. It suggests that the model converges under different prediction steps. As the prediction step increases, the convergent loss increases, indicating that a smaller prediction step results in a higher correlation between the predicted outcomes and the information in the current sample, leading to better model training performance. Conversely, a larger prediction step results in a lower correlation between the predicted outcomes and the information contained in the current sample, leading to poorer model training performance.

Two VIV events are used for testing. Event 1 occurred on April 14, 2019, and Event 2 on July 3, 2021. The predicted results are shown in Figure 24. Observing prediction results of VIV event 1 (Figure 24(a))
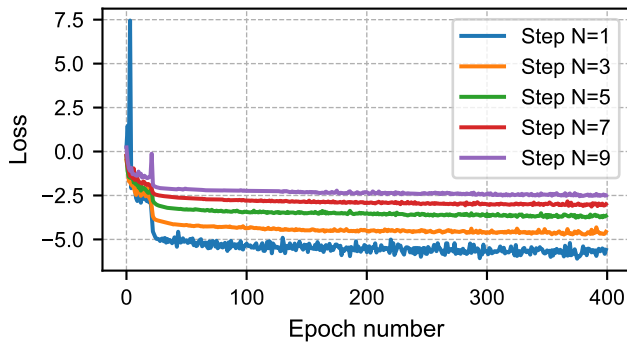
Figure 23: Training loss.

and event 2 (Figure 24(b)). The predicted values with a prediction step size of 1 to 9 minutes have a deviation from the truth, and the trend of the predictions is in line with the actual. As the prediction step size increases, there are instances where the actual values exceed the predicted range. The deviation and the variance (i.e., the uncertainty of the predicted results) between predicted value and the actual value increase with the increase of the prediction step. Larger prediction steps lead to more significant changes in factors such as wind conditions, thereby diminishing the causal relationship between historical features and future index, making it challenging to capture the patterns of structural vibrations. However, from the test results, it is possible to predict the VIV index 5 to 9 minutes in advance, and then predict whether VIV will occur.

VIV amplitude prediction As shown in Section 2.5.2, when predicting that VIV will occur or identifying that VIV has already occurred, to predict the stable amplitude that the structure will converge to, it is necessary to determine the relationship between aerodynamic parameters (Y_1 and ε) and wind speed based on historical VIV data in advance. For the 6th vertical VIV, we selected 8 VIV events with good morphological development (i.e., obvious development, stability, and decaying periods) from historical monitoring data and used the method in Section 2.5.2 to obtain the variations of the aerodynamic parameters Y_1 and ε with wind speed, which are shown in Figures 25(a) and 25(b). The measured stable amplitudes and the computed ones obtained from Equation 40 are presented in Figure 25(c). The computed values are approximately 10% lower than the measured, mainly because the measured stable amplitudes are selected as the maximum values of the response envelope, whereas due to the "peak-and-fall" behavior of the response (see in Figure 18),

the computed stable amplitudes are supposed to be smaller.

To verify the accuracy of calculating the stable amplitude according to the measured wind, we take another 6th order VIV event as an example. The corresponding wind speed for this event is 10.26 m/s. By interpolating from Figures 25(a) and 25(b), we obtain $Y_1 = 7.825$ and $\varepsilon = 319.87$. Consequently, the calculated stable amplitude is 5.326 cm, while the actual amplitude is 8.567 cm. The large prediction deviation can be because the actual variation laws between aerodynamic parameters and wind speed are complicated much more, while the sparse data points in Figure 25 do not adequately reflect this variation law. In fact, the parameters at the same wind speed should follow a certain distribution rather than take a single value. Only when there are sufficient data samples can reliable results be obtained.

3.3. System implementation

Using some of the proposed methods, we developed a VIV monitoring system for Xihoumen Bridge, which has been in operation for approximately two years. The following will introduce some details and the actual effects of the system.

3.3.1. Brief introduction of the system

The VIV monitoring system connects six three-axis anemometers on the bridge deck, two propeller anemometers on the tower, and eight vertical acceleration sensors on the girder from the existing SHM system of the Xihoumen Bridge. The sensor layout is shown in Figure 14. The original monitoring data is transmitted to the local server for real-time analysis, and the analysis results are returned to the front end through a web service interface. The front end visualizes the results and displays them to the user (Figure 26(a)).

Figure 26(b) is the login interface of the system. Figure 26(c) lists the system functions, including:

⌂ **Home page**: used to gather information about VIV. Display the warning level, the time history of the VIV index, the maximum and RMS values of acceleration and dynamic displacement within the past 5 minutes, the average value of wind speed, information on the past three historical VIV events, sensor layout, etc.

📊 **Exhibition of real-time data and analysis**: used to display the measured data and the core analysis results, including:
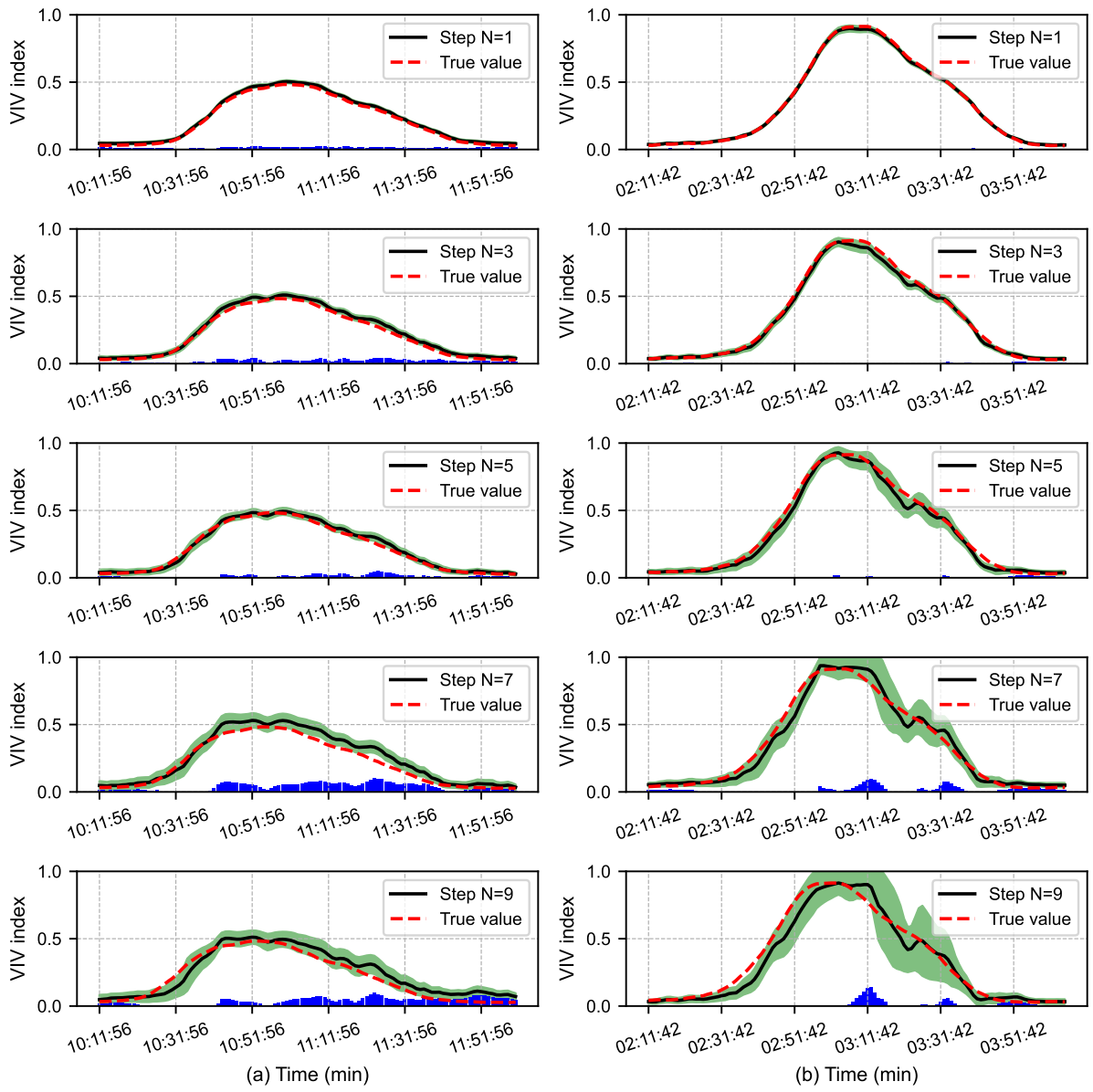
Figure 24: Prediction results of VIV index. (a) VIV event 1 happened on April 14, 2019. (b) VIV event 2 happened on July 3, 2021. (■ represents the prediction interval; ▮ represents the prediction error.)
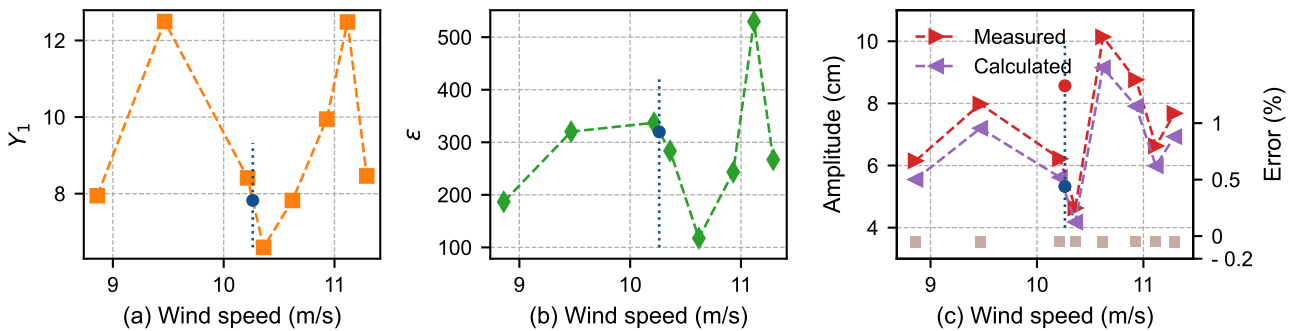
Figure 25: Prediction of VIV stable amplitude. (a) The relationship between Y_1 and U. (b) The relationship between ε and U. (c) The measured and the calculated stable amplitude of VIV. ⫶ corresponds to the wind speed during the VIV event, $U = 10.26$ m/s; ● in (a) and (b) are the interpolated Y_1 and ε; ● and ● in (c) are the amplitude calculated by interpolated Y_1, ε, and wind speed and the measured amplitude.
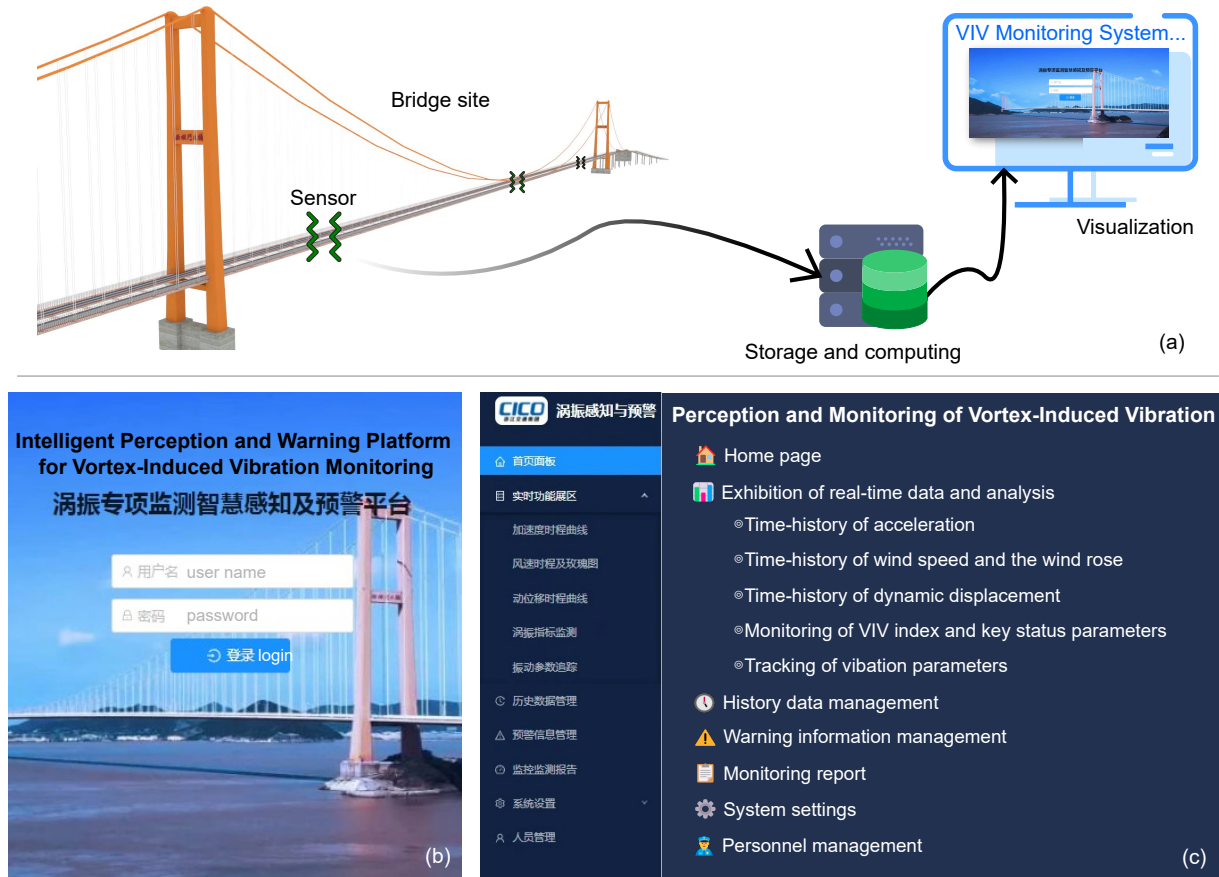
Figure 26: VIV monitoring system and designed functions. (a) Illustration of the VIV monitoring system. (b) Login interface. (c) System functions list.

◎ *Time-history of acceleration*: Display real-time accelerations and statistical box plots of the eight acceleration sensors on the main span, with an update interval of 1 second.

◎ *Time-history of wind speed and the wind rose*: Display real-time wind speed, direction, turbulence, and wind rose plots of six anemometers on the bridge deck and two on the bridge tower. The duration for calculating wind rose and turbulence is 10 minutes, with an update interval of 30 seconds.

◎ *Time-history of dynamic displacement*: Display the real-time dynamic displacement integrated from acceleration and statistical box plots at the eight measurement points, with an update interval of 1 second.

◎ *Monitoring of VIV index and key status parameters*: Display the trajectory and time history of the VIV index at all acceleration

sensors, and the structural status parameters such as amplitude, phase, frequency, and modal shape. Here, the calculation duration is 1 minute, and the update interval is 1 second.

◎ *Tracking of vibration parameters*: Display the spectrum of acceleration, and time history of the first eight instantaneous frequencies and amplitudes at all times (VIV and non-VIV), with a calculation time of 80 seconds and an update interval of 5 seconds.

🕐 **History data management**: used to query and download historical monitoring data.

⚠ **Warning information management**: used to query warning information.

📝 **Monitoring report**: used to generate a VIV report automatically once a VIV event ends. It will record texts such as starting and ending times of VIV, cumulative VIV occurrence times, the

Table 5
Warning levels of VIV.

Level	Light	RMS (mg)	Measure
IV	🔵	<31.5	Keep monitoring
III	🟡	31.5~50	Limit velocity
II	🟠	50~80	Limit velocity and current
I	🔴	>80	Close traffic

maximum amplitude of response, and warning level. It will also record plots such as the time history of acceleration, dynamic displacement, VIV index, instantaneous frequency, instantaneous amplitude, and wind speed.

⚙️ **System settings**: used to set up the system, including system theme customization, VIV warning level management, etc.

👥 **Personnel management**: used to add or remove system administrators, modify permissions, etc.

It can be seen that the main methods used in this monitoring system are VIV identification (Section 2.2) and VIV tracking (Section 2.3). And the methods applied to tracking the instantaneous frequency and amplitude at all times are proposed by the author in [99, 100].

Considering that the VIV index is independent of the amplitude of response, and at present, VIV warning is generally set based on amplitude. We divide VIV events into four levels according to the RMS value of acceleration, as shown in Table 1. So far, no VIV events with Level I and Level II responses have been found according to the monitoring results.

3.3.2. System response to a VIV event

To demonstrate the effectiveness of our system, the following introduced the system response to a specific VIV event. Some results (screenshot of the system) are shown in Figure 27. As we can see, the system identified that the VIV occurred at 16:41:11 pm on August 9, 2022, and the VIV response was classified as Level III (Figure 27(a)). Furthermore, according to the automatically generated VIV report, this VIV event last about 2 hours, with a maximum amplitude of 14.26 cm and a maximum acceleration RMS value of 42.09 mg. Figures 27(b) and 27(c) are the time histories of the VIV index corresponding to the acceleration of all sensors and the trajectory maps of the index at $1/4L$ of the main span at the current time. It can be found that in the current VIV situation, as expected, the value of the VIV index is close to 1, and as expected, the trajectory on the complex plane converges to a circle.

In fact, since its operation, the system has successfully captured multiple VIV events, providing powerful support to bridge maintenance personnel for timely detection of VIV, understanding structural conditions in real-time, retrospective analysis, and making informed and scientific decisions. The accumulated VIV data also offer valuable on-site measurements for further research on bridge VIV.

4. Discussion

4.1. On VIV identification-tracking-evaluation

The response of bridge VIV can reach tens of centimeters or only a few centimeters. Although the R index can accurately identify VIV at different vibration levels, it also implies that large and small VIVs are indistinguishable in terms of the R index, making it unsuitable for direct decision-making. Because for VIV at different levels, it is clear that they should be treated differently. In our system implementation, the different levels of VIV warning are still divided by the magnitude of vibration acceleration or displacement, which should be explored deeper. To this end, we propose a solution that evaluates and categorizes VIV considering vibration-based driving comfort and vision-based driving safety. We have made initial progress in getting through relevant computational aspects. However, the factors considered in this article are not comprehensive enough. For example, when calculating the OVTV, we only considered the vertical acceleration transmitted from the bridge to the vehicle, neglecting inputs from other DOFs and the influence of road roughness, which will lead to underestimating the impact of VIV on divers.

4.2. On VIV prediction

In Section 2.5, we utilize the statistical characteristics of the wind field to determine whether VIV will occur. However, this paper only considers the statistical laws of wind speed and direction without considering other influencing factors such as wind attack angle and turbulence intensity. This limitation leads to inaccurate predictions of VIV. Specifically, it results in a higher false-positive rate. Macdonald et al.'s analysis of VIVs of the Second Seven Crossing Bridge [47] showed that when wind speed and direction locked into the so-called VIV range, only 16% of the time that VIV occurs, indicating the necessity for additional factors to trigger VIV. In this paper, on the basis of determining the occurrence of VIV according to wind speed and direction, we utilize a neural network to predict the VIV
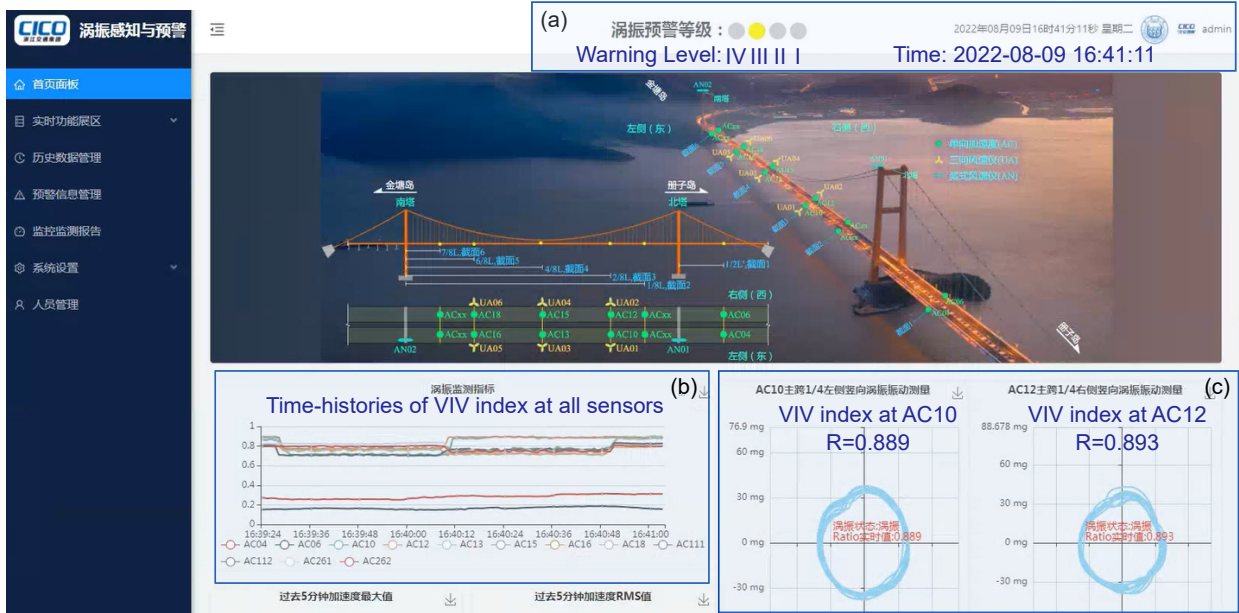
Figure 27: System response to a VIV event. (a) Warning level. (b) The time history of the VIV index of all sensors. (c) The VIV index of sensors AC10 and AC12.

index and judge again whether VIV will occur, which can improve the accuracy of VIV prediction. However, the feature vectors of the samples used to train the neural network still only consider wind speed and direction in terms of the wind field. In future research, it is essential to incorporate factors such as wind attack angle and turbulence intensity into the feature space. Similarly, when predicting the stable amplitude of VIV, these factors should also be included as independent variables in the aerodynamic parameters.

In addition, increasing the sample size will significantly benefit the accuracy of VIV occurrence prediction and stable amplitude prediction. Utilizing our developed VIV monitoring system, VIV events can be detected and saved promptly, allowing for the continuous accumulation of VIV data samples and updates to the database and related models.

When using the method proposed in Section 2.5.2 to calculate the stable amplitude of VIV, to obtain accurate relationships between aerodynamic parameters and wind speed, the developmental shape of VIV response must conform to a trend of [exponential growth]-[stable plateau]-[exponential decay]. Otherwise, it will lead to imprecise parameter fitting results and affect the accuracy of amplitude prediction.

4.3. On construction of VIV monitoring system

At present, the VIV monitoring system we established primarily focuses on VIV identification and structural status tracking. And the research content in

the paper on VIV evaluation, VIV occurrence prediction, and VIV stable amplitude prediction has not been integrated into the system. We will consider implementing these functionalities online in the future. The monitoring system exhibits good versatility, which can be applied to other structures prone to VIV, such as cables/hangers of bridges, towers, and offshore wind turbines.

5. Conclusion

In response to the frequent occurrence of VIV during the operation of long-span bridges and the necessity of monitoring it, this paper presents a comprehensive scheme for intelligent VIV perception and prediction and provides corresponding technical implementations. It focuses on the real-time identification of VIV, online tracking of structural key state parameters during VIV, and driving evaluation based on comfort and safety. Meanwhile, it explored the prediction of VIV occurrence in advance and the estimation of VIV stable amplitude. Feasibility of the proposed methods is verified through the historical VIV data of two long-span suspension bridges. Furthermore, a VIV monitoring system for one of the bridges is established based on the proposed VIV identification and tracking methods. Effectiveness of the system is confirmed by practices. It plays a positive and significant role in structural maintenance and management.

Monitoring-based VIV perception (identification-tracking-evaluation) and prediction can significantly aid bridge managers in responding to VIV events promptly, calmly, and reasonably. Moreover, it can enhance the comprehension of structural VIVs. Research in this field involves knowledge and technology in multiple domains, such as fluid mechanics, structural mechanics, and control theory. Future research on VIV needs to expand interdisciplinary cooperation while combining field measurements and numerical simulations to promote the solution to VIV issues in engineering structures. The ultimate objective of structural VIV monitoring is not solely to observe but to precisely control it. Current control methods for VIV are mainly passive and manually intervened, which suffer from obvious time-lag and are hard to suppress VIV responses effectively. Intelligent and adaptive control based on monitoring information feedback hold promising potential for playing a crucial role in addressing bridge VIV control problems.

Due to space limitations, the author cannot elaborate on the details of each method and consolidate them into a single article (although this article is no longer short). Therefore, the focus of this article is to provide a comprehensive picture of the proposed technical framework of intelligent perception and prediction for bridge VIV and concise descriptions of the methods used, ensuring consistency and readability of the paper. More detailed explanations of VIV prediction and evaluation will be presented in subsequent articles.

6. Acknowledgments

CRediT authorship contribution statement

Danhui Dan: Conceptualization, Methodology, Writing - original draft, Validation, Formal analysis, Supervision, Project administration, Funding acquisition, Resource. **Xuewen Yu:** Conceptualization, Methodology, Software, Formal analysis, Investigation, Writing - original draft, Writing - review & editing, Visualization, Project administration. **Houjin Li:** Methodology, Software, Formal analysis, Investigation. **Gang Zeng:** Methodology, Software, Formal analysis, Investigation. **Chenqi Wang:** Methodology, Software, Formal analysis, Investigation. **Hua Guan:** Data Curation, Investigation.

References

[1] T. Wu, A. Kareem, An overview of vortex-induced vibration (VIV) of bridge decks, Frontiers of Structural and Civil Engineering 6 (4) (2012) 335–347. doi:10.1007/s11709-012-0179-1.

[2] Y. Ge, L. Zhao, J. Cao, Case study of vortex-induced vibration and mitigation mechanism for a long-span suspension bridge, Journal of Wind Engineering and Industrial Aerodynamics 220 (2022) 104866. doi:10.1016/j.jweia.2021.104866.

[3] L. Zhao, W. Cui, X. Shen, S. Xu, Y. Ding, Y. Ge, A fast on-site measure-analyze-suppress response to control vortex-induced-vibration of a long-span bridge, Structures 35 (2022) 192–201. doi:10.1016/j.istruc.2021.10.017.

[4] A. S. Corriols, G. Morgenthal, Computational analysis of viv observed on existing bridges, in: The seventh international colloquium on bluff body aerodynamics and applications (BBAA7), Shanghai, China, 2012.

[5] Y. Fujino, Y. Yoshida, Wind-Induced Vibration and Control of Trans-Tokyo Bay Crossing Bridge, Journal of Structural Engineering 128 (8) (2002) 1012–1025. doi:10.1061/(ASCE)0733-9445(2002)128:8(1012).

[6] Y. C. Hwang, S. Kim, H.-K. Kim, Cause investigation of high-mode vortex-induced vibration in a long-span suspension bridge, Structure and Infrastructure Engineering 16 (1) (2020) 84–93. doi:10.1080/15732479.2019.1604771.

[7] H.-W. Zhao, Y.-L. Ding, A.-Q. Li, X.-W. Liu, B. Chen, J. Lu, Evaluation and Early Warning of Vortex-Induced Vibration of Existed Long-Span Suspension Bridge Using Multisource Monitoring Data, Journal of Performance of Constructed Facilities 35 (3) (2021) 04021007. doi:10.1061/(ASCE)CF.1943-5509.0001571.

[8] D. Dan, X. Yu, F. Han, B. Xu, Research on dynamic behavior and traffic management decision-making of suspension bridge after vortex-induced vibration event, Structural Health Monitoring 21 (3) (2022) 872–886.

[9] H. Li, S. Laima, Q. Zhang, N. Li, Z. Liu, Field monitoring and validation of vortex-induced vibrations of a long-span suspension bridge, Journal of Wind Engineering and Industrial Aerodynamics 124 (2014) 54–67. doi:10.1016/j.jweia.2013.11.006.

[10] M. Jafari, F. Hou, A. Abdelkefi, Wind-induced vibration of structural cables, Nonlinear Dynamics 100 (2020) 351–421.

[11] S. Kim, S. Kim, H.-K. Kim, High-mode vortex-induced vibration of stay cables: Monitoring, cause investigation, and mitigation, Journal of Sound and Vibration 524 (2022) 116758. doi:10.1016/j.jsv.2022.116758.

[12] S. Arunachalam, N. Lakshmanan, Non-linear modelling of vortex induced lock-in effects on circular chimneys, Journal of Wind Engineering and Industrial Aerodynamics 202 (2020) 104201. doi:10.1016/j.jweia.2020.104201.

[13] X. Fu, Y. Jiang, H.-N. Li, J.-X. Li, W.-P. Xie, L.-D. Yang, J. Zhang, Vortex-Induced Vibration and Countermeasure of a Tubular Transmission Tower, International Journal of Structural Stability and Dynamics 21 (12) (2021) 2150163. doi:10.1142/S0219455421501637.

[14] J. C. Heinz, N. N. Sørensen, F. Zahle, W. Skrzypiński, Vortex-induced vibrations on a modern wind turbine blade, Wind Energy 19 (11) (2016) 2041–2051. doi:10.1002/we.1967.

[15] D. W. Carlson, Y. Modarres-Sadeghi, Vortex-induced vibration of spar platforms for floating offshore wind turbines, Wind Energy 21 (11) (2018) 1169–1176. doi:10.1002/we.2221.

[16] D. Yin, E. Passano, F. Jiang, H. Lie, J. Wu, N. Ye, S. Sævik, B. J. Leira, State-of-the-Art Review of Vortex-Induced Motions of Floating Offshore Wind Turbine Structures, Journal of Marine Science and Engineering 10 (8) (2022) 1021. doi:10.3390/jmse10081021.

[17] K.-S. Hong, U. H. Shah, Vortex-induced vibrations and control of marine risers: A review, Ocean Engineering 152 (2018) 300–315. doi:10.1016/j.oceaneng.2018.01.086.

[18] G. Liu, H. Li, Z. Qiu, D. Leng, Z. Li, W. Li, A mini review of recent progress on vortex-induced vibrations of marine risers, Ocean Engineering 195 (2020) 106704. doi:10.1016/j.oceaneng.2019.106704.

[19] X. Yiqiang, C. Chunfeng, Vortex-Induced Dynamic Response Analysis for the Submerged Floating Tunnel System under the Effect of Currents, Journal of Waterway, Port, Coastal, and Ocean Engineering 139 (3) (2013) 183–189. doi:10.1061/(ASCE)WW.1943-5460.0000175.

[20] D. Wang, Y. Chen, Z. Hao, Q. Cao, Bifurcation analysis for vibrations of a turbine blade excited by air flows, Science China Technological Sciences 59 (8) (2016) 1217–1231. doi:10.1007/s11431-016-6064-8.

[21] S. Di Nino, A. Luongo, Nonlinear interaction between self- and parametrically excited wind-induced vibrations, Nonlinear Dynamics 103 (1) (2021) 79–101. doi:10.1007/s11071-020-06114-3.

[22] S. Cao, Y. Zhang, H. Tian, R. Ma, W. Chang, A. Chen, Drive comfort and safety evaluation for vortex-induced vibration of a suspension bridge based on monitoring data, Journal of Wind Engineering and Industrial Aerodynamics 204 (2020) 104266. doi:10.1016/j.jweia.2020.104266.

[23] J. Zhu, Z. Xiong, H. Xiang, X. Huang, Y. Li, Ride comfort evaluation of stochastic traffic flow crossing long-span suspension bridge experiencing vortex-induced vibration, Journal of Wind Engineering and Industrial Aerodynamics 219 (2021) 104794. doi:10.1016/j.jweia.2021.104794.

[24] D. Gao, Z. Deng, W. Yang, W. Chen, Review of the excitation mechanism and aerodynamic flow control of vortex-induced vibration of the main girder for long-span bridges: A vortex-dynamics approach, Journal of Fluids and Structures 105 (2021) 103348. doi:10.1016/j.jfluidstructs.2021.103348.

[25] J. Frandsen, Comparison of numerical prediction and full-scale measurements of vortex induced oscillations, in: Proceedings of the 4th International Colloquium on Bluff Body Aerodynamics and Applications, Ruhu-University of Bochum, Bochum, Germany, 2000, pp. 11–14.

[26] S. Laima, H. Li, W. Chen, J. Ou, Effects of attachments on aerodynamic characteristics and vortex-induced vibration of twin-box girder, Journal of Fluids and Structures 77 (2018) 115–133. doi:10.1016/j.jfluidstructs.2017.12.005.

[27] F. Wu, Z. Wang, L. Zhao, T. Pan, H. Xiao, Y. Ge, Aerodynamic force distribution characteristics around a double-slotted box girder of a long-span bridge during vortex-induced vibration, Journal of Bridge Engineering 28 (1) (2023) 04022132.

[28] E. Simiu, R. H. Scanlan, Wind effects on structures: fundamentals and applications to design, Vol. 688, John Wiley New York, 1996.

[29] F. Ehsan, R. H. Scanlan, Vortex-Induced Vibrations of Flexible Bridges, Journal of Engineering Mechanics 116 (6) (1990) 1392–1411. doi:10.1061/(ASCE)0733-9399(1990)116:6(1392).

[30] A. M. Marra, C. Mannini, G. Bartoli, Van der Pol-type equation for modeling vortex-induced oscillations of bridge decks, Journal of Wind Engineering and Industrial Aerodynamics 99 (6) (2011) 776–785. doi:10.1016/j.jweia.2011.03.014.

[31] L.-D. Zhu, X.-L. Meng, L.-Q. Du, M.-C. Ding, A Simplified Nonlinear Model of Vertical Vortex-Induced Force on Box Decks for Predicting Stable Amplitudes of Vortex-Induced Vibrations, Engineering 3 (6) (2017) 854–862. doi:10.1016/j.eng.2017.06.001.

[32] Q. Zhu, Y. L. Xu, L. D. Zhu, B. Y. Chen, A semi-empirical model for vortex-induced vertical forces on a twin-box deck under turbulent wind flow, Journal of Fluids and Structures 71 (2017) 183–198. doi:10.1016/j.jfluidstructs.2017.03.011.

[33] L.-D. Zhu, X.-L. Meng, L.-Q. Du, M.-C. Ding, A simplified nonlinear model of vertical vortex-induced force on box decks for predicting stable amplitudes of vortex-induced vibrations, Engineering 3 (6) (2017) 854–862.

[34] G. Gao, L. Zhu, J. Li, W. Han, Application of a new empirical model of nonlinear self-excited force to torsional vortex-induced vibration and nonlinear flutter of bluff bridge sections, Journal of Wind Engineering and Industrial Aerodynamics 205 (2020) 104313. doi:10.1016/j.jweia.2020.104313.

[35] H. Sun, L.-D. Zhu, Q. Zhu, C. Qian, X.-L. Meng, L.-Q. Du, Identification of parameters for same-order nonlinear damping terms in polynomial-type vortex-induced force models for bridge decks, Journal of Wind Engineering and Industrial Aerodynamics 229 (2022) 105158. doi:10.1016/j.jweia.2022.105158.

[36] C. M. Cheng, Volterra-series-based nonlinear system modeling and its engineering applications_ A state-of-the-art review, Mechanical Systems and Signal Processing (2017). doi:10.1016/j.ymssp.2016.10.029.

[37] T. Wu, A. Kareem, Vortex-Induced Vibration of Bridge Decks: Volterra Series-Based Model, Journal of Engineering Mechanics 139 (12) (2013) 1831–1843. doi:10.1061/(ASCE)EM.1943-7889.0000628.

[38] T. Wu, A. Kareem, Simulation of nonlinear bridge aerodynamics: A sparse third-order Volterra model, Journal of Sound and Vibration 333 (1) (2014) 178–188. doi:10.1016/j.jsv.2013.09.003.

[39] K. Xu, L. Zhao, Y. Ge, Reduced-order modeling and calculation of vortex-induced vibration for large-span bridges, Journal of Wind Engineering and Industrial Aerodynamics 167 (2017) 228–241. doi:10.1016/j.jweia.2017.04.016.

[40] S. L. Brunton, J. L. Proctor, J. N. Kutz, Discovering governing equations from data by sparse identification of nonlinear dynamical systems, Proceedings of the National Academy of Sciences 113 (15) (2016) 3932–3937. doi:10.1073/pnas.1517384113.

[41] B. Lusch, J. N. Kutz, S. L. Brunton, Deep learning for universal linear embeddings of nonlinear dynamics, Nature Communications 9 (1) (2018) 4950. doi:10.1038/s41467-018-07210-0.

[42] K. Champion, B. Lusch, J. N. Kutz, S. L. Brunton, Data-driven discovery of coordinates and governing equations, Proceedings of the National Academy of Sciences 116 (45) (2019) 22445–22451. doi:10.1073/pnas.1906995116.

[43] N. Geneva, N. Zabaras, Modeling the dynamics of PDE systems with physics-constrained deep auto-regressive networks, Journal of Computational Physics 403 (2020) 109056. doi:10.1016/j.jcp.2019.109056.

[44] M. Kalia, S. L. Brunton, H. G. E. Meijer, C. Brune, J. N. Kutz, Learning normal form autoencoders for data-driven discovery of universal,parameter-dependent governing equations (2021). arXiv:arXiv:2106.05102.

[45] S. Li, E. Kaiser, S. Laima, H. Li, S. L. Brunton, J. N. Kutz, Discovering time-varying aerodynamics of a prototype bridge by sparse identification of nonlinear dynamical systems, Physical Review E 100 (2) (2019) 022220. doi:10.1103/PhysRevE.100.022220.

[46] T. Ma, W. Cui, T. Gao, S. Liu, L. Zhao, Y. Ge, Data-based autonomously discovering method for nonlinear aerodynamic force of quasi-flat plate, Physics of Fluids 35 (2) (2023) 024103. doi:10.1063/5.0133526.

[47] J. H. G. Macdonald, P. A. Irwin, M. S. Fletcher, Vortex-induced vibrations of the Second Severn Crossing cable-stayed bridge—full-scale and wind tunnel measurements, Proceedings of the Institution of Civil Engineers - Structures and Buildings 152 (2) (2002) 123–134. doi:10.1680/stbu.2002.152.2.123.

[48] A. Larsen, S. Esdahl, J. E. Andersen, T. Vejrum, Storebælt suspension bridge–vortex shedding excitation and mitigation by guide vanes, Journal of Wind Engineering and Industrial Aerodynamics 88 (2-3) (2000) 283–296.

[49] J.-W. Seo, H.-K. Kim, J. Park, K.-T. Kim, G.-N. Kim, Interference effect on vortex-induced vibration in a parallel twin cable-stayed bridge, Journal of Wind Engineering and Industrial Aerodynamics 116 (2013) 7–20. doi:10.1016/j.jweia.2013.01.014.

[50] D. Dan, H. Li, Monitoring, intelligent perception, and early warning of vortex-induced vibration of suspension bridge, Structural Control and Health Monitoring 29 (5) (2022) e2928. doi:10.1002/stc.2928.

[51] C. R. Farrar, K. Worden, An introduction to structural health monitoring, Philosophical Transactions of the Royal Society A: Mathematical, Physical and Engineering Sciences 365 (1851) (2007) 303–315.

[52] V. R. Gharehbaghi, E. Noroozinejad Farsangi, M. Noori, T. Yang, S. Li, A. Nguyen, C. Málaga-Chuquitaype, P. Gardoni, S. Mirjalili, A critical review on structural health monitoring: Definitions, methods, and perspectives, Archives of Computational Methods in Engineering (2021) 1–27.

[53] Z. He, W. Li, H. Salehi, H. Zhang, H. Zhou, P. Jiao, Integrated structural health monitoring in bridge engineering, Automation in Construction 136 (2022) 104168.

[54] D. Pines, A. E. Aktan, Status of structural health monitoring of long-span bridges in the united states, Progress in Structural Engineering and materials 4 (4) (2002) 372–380.

[55] J. Ou, H. Li, Structural health monitoring in mainland china: review and future trends, Structural health monitoring 9 (3) (2010) 219–231.

[56] D. Inaudi, Overview of 40 bridge structural health monitoring projects, in: International bridge conference, IBC, 2010, pp. 15–17.

[57] Y. Fujino, D. M. Siringoringo, Y. Ikeda, T. Nagayama, T. Mizutani, Research and implementations of structural monitoring for bridges and buildings in japan, Engineering 5 (6) (2019) 1093–1119.

[58] S. Li, S. Laima, H. Li, Cluster analysis of winds and wind-induced vibrations on a long-span bridge based on long-term field monitoring data, Engineering Structures 138 (2017) 245–259. doi:10.1016/j.engstruct.2017.02.024.

[59] Z. Huang, Y. Li, X. Hua, Z. Chen, Q. Wen, Automatic Identification of Bridge Vortex-Induced Vibration Using Random Decrement Method, Applied Sciences 9 (10) (2019) 2049. doi:10.3390/app9102049.

[60] S. Xu, R. Ma, D. Wang, A. Chen, H. Tian, Prediction analysis of vortex-induced vibration of long-span suspension bridge based on monitoring data, Journal of Wind Engineering and Industrial Aerodynamics 191 (2019) 312–324. doi:10.1016/j.jweia.2019.06.016.

[61] J. Lim, S. Kim, H.-K. Kim, Using supervised learning techniques to automatically classify vortex-induced vibration in long-span bridges, Journal of Wind Engineering and Industrial Aerodynamics 221 (2022) 104904. doi:10.1016/j.jweia.2022.104904.

[62] J. Zhang, L. Zhou, Y. Tian, S. Yu, W. Zhao, Y. Cheng, Vortex-induced vibration measurement of a long-span suspension bridge through noncontact sensing strategies, Computer-Aided Civil and Infrastructure Engineering 37 (12) (2022) 1617–1633. doi:10.1111/mice.12712.

[63] S. Li, S. Laima, H. Li, Physics-guided deep learning framework for predictive modeling of bridge vortex-induced vibrations from field monitoring, Physics of Fluids 33 (3) (2021) 037113. doi:10.1063/5.0032402.

[64] W. E, A Proposal on Machine Learning via Dynamical Systems, Communications in Mathematics and Statistics 5 (1) (2017) 1–11. doi:10/ggrtrp.

[65] T. Q. Chen, Y. Rubanova, J. Bettencourt, D. K. Duvenaud, Neural Ordinary Differential Equations, in: NuerIPS, 2018, p. 13.

[66] Q. Zhu, Y. Xu, L. Zhu, H. Li, Vortex-induced vibration analysis of long-span bridges with twin-box decks under non-uniformly distributed turbulent winds, Journal of Wind Engineering and Industrial Aerodynamics 172 (2018) 31–41. doi:10.1016/j.jweia.2017.11.005.

[67] P. Liu, X. Chu, W. Cui, L. Zhao, Y. Ge, Bayesian inference based parametric identification of vortex-excited force using on-site measured vibration data on a long-span bridge, Engineering Structures 266 (2022) 114597. doi:10.1016/j.engstruct.2022.114597.

[68] S. Kim, J. Park, H.-K. Kim, Damping Identification and Serviceability Assessment of a Cable-Stayed Bridge Based on Operational Monitoring Data, Journal of Bridge Engineering 22 (3) (2017) 04016123. doi:10.1061/(ASCE)BE.1943-5592.0001004.

[69] D. Xin, J. Zhan, H. Zhang, J. Ou, Control of Vortex-Induced Vibration of a Long-Span Bridge by Inclined Railings, Journal of Bridge Engineering 26 (12) (2021) 04021093. doi:10.1061/(ASCE)BE.1943-5592.0001803.

[70] J. Zhan, D. Xin, J. Ou, Z. Liu, Experimental study on suppressing vortex-induced vibration of a long-span bridge by installing the wavy railings, Journal of Wind Engineering and Industrial Aerodynamics 202 (2020) 104205. doi:10.1016/j.jweia.2020.104205.

[71] Z. Xue, B. Han, H. Zhang, D. Xin, J. Zhan, R. Wang, External suction-blowing method for controlling vortex-induced vibration of a bridge, Journal of Wind Engineering and Industrial Aerodynamics 215 (2021) 104661. doi:10.1016/j.jweia.2021.104661.

[72] C. Zheng, T. Ji, F. Xie, X. Zhang, H. Zheng, Y. Zheng, From active learning to deep reinforcement learning: Intelligent active flow control in suppressing vortex-induced vibration, Physics of Fluids 33 (6) (2021) 063607. doi:10.1063/5.0052524.

[73] G.-B. Chen, W.-L. Chen, D.-L. Gao, Z.-F. Yang, Active control of flow structure and unsteady aerodynamic force of box girder with leading-edge suction and trailing-edge jet, Experimental Thermal and Fluid Science 120 (2021) 110244. doi:10.1016/j.expthermflusci.2020.110244.

[74] J. Dai, Z.-D. Xu, P.-P. Gai, Z.-W. Hu, Optimal design of tuned mass damper inerter with a Maxwell element for mitigating the vortex-induced vibration in bridges, Mechanical Systems and Signal Processing 148 (2021) 107180. doi:10.1016/j.ymssp.2020.107180.

[75] H. Yu, O. Øiseth, M. Zhang, F. Xu, G. Hu, Tuned Mass Damper Design for Vortex-Induced Vibration Control of a Bridge: Influence of Vortex-Induced Force Model, Journal of Bridge Engineering 28 (5) (2023) 04023021. doi:10.1061/JBENF2.BEENG-5958.

[76] A. Patil, S. Jung, S. Lee, S.-D. Kwon, Mitigation of vortex-induced vibrations in bridges under conflicting objectives, Journal of Wind Engineering and Industrial Aerodynamics 99 (12) (2011) 1243–1252. doi:10.1016/j.jweia.2011.10.001.

[77] J. Dai, Z.-D. Xu, S. J. Dyke, Robust control of vortex-induced vibration in flexible bridges using an active tuned mass damper, Structural Control and Health Monitoring 29 (8) (2022) e2980. doi:10.1002/stc.2980.

[78] A. Buljac, H. Kozmar, S. Pospíšil, M. Macháček, Aerodynamic and aeroelastic characteristics of typical bridge decks equipped with wind barriers at the windward bridge-deck edge, Engineering Structures 137 (2017) 310–322. doi:10.1016/j.engstruct.2017.01.055.

[79] R. Naseer, H. L. Dai, A. Abdelkefi, L. Wang, Piezomagnetoelastic energy harvesting from vortex-induced vibrations using monostable characteristics, Applied Energy 203 (2017) 142–153. doi:10.1016/j.apenergy.2017.06.018.

[80] S. M. Hasheminejad, A. H. Rabiee, A. H. D. Markazi, Dual-Functional Electromagnetic Energy Harvesting and Vortex-Induced Vibration Control of an Elastically Mounted Circular Cylinder, Journal of Engineering Mechanics 144 (3) (2018) 04017184. doi:10.1061/(ASCE)EM.1943-7889.0001411.

[81] B. H. Huynh, T. Tjahjowidodo, Z. W. Zhong, Y. Wang, N. Srikanth, Design and experiment of controlled bistable vortex induced vibration energy harvesting systems operating in chaotic regions, Mechanical Systems and Signal Processing 98 (2018) 1097–1115.

doi:10.1016/j.ymssp.2017.06.002.

[82] A. G.A Muthalif, M. Hafizh, J. Renno, M. R. Paurobally, A hybrid piezoelectric-electromagnetic energy harvester from vortex-induced vibrations in fluid-flow; the influence of boundary condition in tuning the harvester, Energy Conversion and Management 256 (2022) 115371. doi:10.1016/j.enconman.2022.115371.

[83] L. Zhang, B. Meng, Y. Tian, X. Meng, X. Lin, Y. He, C. Xing, H. Dai, L. Wang, Vortex-induced vibration triboelectric nanogenerator for low speed wind energy harvesting, Nano Energy 95 (2022) 107029. doi:10.1016/j.nanoen.2022.107029.

[84] J. Wang, L. Geng, L. Ding, H. Zhu, D. Yurchenko, The state-of-the-art review on energy harvesting from flow-induced vibrations, Applied Energy 267 (2020) 114902. doi:10.1016/j.apenergy.2020.114902.

[85] S. Farhangdoust, A. Mehrabi, D. Younesian, Bistable wind-induced vibration energy harvester for self-powered wireless sensors in smart bridge monitoring systems, in: Nondestructive Characterization and Monitoring of Advanced Materials, Aerospace, Civil Infrastructure, and Transportation XIII, Vol. 10971, SPIE, 2019, pp. 53–60. doi:10.1117/12.2517424.

[86] H. Kanamori, P. Maechling, E. Hauksson, Continuous monitoring of ground-motion parameters, Bulletin of the Seismological Society of America 89 (1) (1999) 311–316.

[87] J. L. Shanks, Recursion filters for digital processing, Geophysics 32 (1) (1967) 33–51.

[88] W. Zheng, D. Dan, W. Cheng, Y. Xia, Real-time dynamic displacement monitoring with double integration of acceleration based on recursive least squares method, Measurement 141 (2019) 460–471. doi:10.1016/j.measurement.2019.04.053.

[89] K. Dragomiretskiy, D. Zosso, Variational mode decomposition, IEEE transactions on signal processing 62 (3) (2013) 531–544.

[90] N. E. Huang, Z. Shen, S. R. Long, M. C. Wu, H. H. Shih, Q. Zheng, N.-C. Yen, C. C. Tung, H. H. Liu, The empirical mode decomposition and the hilbert spectrum for nonlinear and non-stationary time series analysis, Proceedings of the Royal Society of London. Series A: mathematical, physical and engineering sciences 454 (1971) (1998) 903–995.

[91] J. Gilles, Empirical wavelet transform, IEEE transactions on signal processing 61 (16) (2013) 3999–4010.

[92] Y. Zhou, C. Suren, Vehicle ride comfort analysis with whole-body vibration on long-span bridges subjected to crosswind, Journal of Wind Engineering and Industrial Aerodynamics 155 (2016) 126–140. doi:10.1016/j.jweia.2016.05.001.

[93] J. Zhu, W. Zhang, M. Wu, Evaluation of ride comfort and driving safety for moving vehicles on slender coastal bridges, Journal of Vibration and Acoustics 140 (5) (2018).

[94] The MathWorks Inc., Curve fitting toolbox (2022). URL https://www.mathworks.com/help/curvefit/index.html

[95] ISO 2631-1:1997 mechanical vibration and shock evaluation of human exposure to whole-body vibration part 1: General requirements, International Organization for Standardization, Geneva (1997).

[96] The MathWorks Inc., Optimization toolbox (2022). URL https://www.mathworks.com/help/optim/index.html

[97] L. Kong, J. Sun, C. Zhang, SDE-Net: Equipping Deep Neural Networks with Uncertainty Estimates (2020). arXiv:2008.10546.

[98] L. Chen, Z. Liu, S. Nagarajaiah, L. Sun, L. Zhao, W. Cui, Vibration mitigation of long-span bridges with damped outriggers, Engineering Structures 271 (2022) 114873.

[99] X. Yu, D. Dan, Block-wise recursive APES aided with frequency-squeezing postprocessing and the application in online analysis of vibration monitoring signals, Mechanical Systems and Signal Processing 162 (2022) 108063. doi:10.1016/j.ymssp.2021.108063.

[100] X. Yu, D. Dan, Online frequency and amplitude tracking in structural vibrations under environment using APES spectrum postprocessing and Kalman filtering, Engineering Structures 259 (2022) 114175. doi:10.1016/j.engstruct.2022.114175.